CHANGES IN ION ORBIT LOSS, INTRINSIC ROTATION AND PARTICLE PINCH ACROSS THE L-H TRANSITION IN DIII-D PLASMAS

A Thesis
Presented to
The Academic Faculty

By

Nicholas A. Piper

In Partial Fulfillment
of the Requirements for the Degree
Master of Science in
Nuclear and Radiological Engineering

Georgia Institute of Technology

May 2018

CHANGES IN ION ORBIT LOSS, INTRINSIC ROTATION AND PARTICLE PINCH ACROSS THE L-H TRANSITION IN DIII-D PLASMAS

Approved by:

Dr. W.M. Stacey, Advisor
Nuclear and Radiological Engineering
Georgia Institute of Technology

Dr. Richard J. Groebner
Senior Technical Advisor
General Atomics Pedestal and ELM Control Group

Dr. Bojan Petrovic
Nuclear and Radiological Engineering
Georgia Institute of Technology

Date Approved: March 15, 2018

ACKNOWLEDGEMENTS

Thanks goes out to Dr. R. J. Groebner for his insight in fitting the experimental data. He has aided me greatly in my understanding of the DIII-D tools and the MDSPlus database. Thanks goes out to Dr. Grierson for his help regarding the CER system and deuterium data. I would also like to thank Dr. J. P. Floyd II for teaching me to use the DIII-D tools. Thanks goes to Dr. T. M. Wilks and Max Hill for their contributions to my understanding of ion orbit loss. I wish to thank Dr. Stacey for his guidance, support, and patience. I could not ask for a better advisor. I appreciate my family for supporting me and being proud of me, even when I didn't think I deserved it.

Lastly, I wish to thank my committee members for their time and contributions to the advancement of human knowledge.

This material is based upon work supported by the U.S. Department of Energy, Office of Science, Office of Fusion Energy Sciences, using the DIII-D National Fusion Facility, a DOE Office of Science user facility, under Awards DE-FC02-04ER54698.

TABLE OF CONTENTS

LIST OF TABLES

LIST OF FIGURES

SUMMARY

Some thermalized ions flowing slowly radially outward have sufficient energy to access loss orbits which allow them to free stream out of the confined plasma region and become ion orbit lost (IOL). Ions flowing in the counter-current (ctr-I_p) direction are more readily lost, exerting a net torque on the ions in the co-current direction. A particle-momentum-energy balance analysis, including the effects of IOL, was performed on three similar DIII-D discharges. After the L-H transition, the intrinsic rotation due to IOL decreases for a short time in the plasma edge near the separatrix. For 1 of the 3 discharges, there is a corresponding decrease in the measured carbon rotation in the edge. For all of the discharges, the electromagnetic pinch velocity went from weakly inward in L-mode to strongly inward in H-mode near the separatrix.

CHAPTER 1
BACKGROUND

As the global population continues to rise, the demand for a plentiful and efficient means of generating power will only increase. The Paris Agreement [1] displays an international effort to reduce global emissions and invest in alternative sources of carbon-free energy, such as wind, solar, hydroelectric, geothermal, and nuclear. Unfortunately, wind and solar power are not reliably generated, as they depend on the wind speed and time of day. Other sources of clean energy produce little power relative to the demands of the global population. The advantage of nuclear power is that it has the potential to generate large amounts of energy, while also achieving extremely high energy density relative to other sources of clean energy. This makes nuclear technology an attractive means of reaching the base load power for the electrical grid. While energy generated from fission reactors is used commercially today, fusion does not produce long lasting radionuclides, and its fuel can be found in seawater, drastically increasing the total amount of fuel that can be found on Earth.

1.1 Fusion Basics

Nuclear energy is produced by fusion through the process of combining two low mass nuclei together. They interact with each other to produce a compound nucleus. The difference between the mass of the reactants and products is converted into energy, and eventually, heat. However, as two nuclei approach one another, the electric field between them exerts a massive repulsive force, causing them to scatter rather than fuse. In most cases, there is a minimum energy required for two nuclei to get close enough to fuse. This is known as the Coulomb barrier. To achieve a high fusion reaction rate, the atoms must be heated to a kinetic temperature in the KeV range, which is on the order of 10,000,000 K or greater. Figure 1.1 [2] shows the reactivities of different fusion reactions as a function of energy,

represented as temperature.

The reaction expected to be utilized in first generation fusion reactors is the D-T reaction, combining a deuterium (D, H-2) and tritium (T, H-3) nucleus to produce a helium nucleus and a neutron, as shown below.

$D_1^2 + T_1^3 \rightarrow He_2^4 + n_0^1 + 17.6MeV$

We can see from Fig. 1.1 that the D-T reaction possesses a significantly higher reactivity relative to the D-D reaction, making it much more promising for power generation. However, tritium is costly to produce relative to deuterium, and is also radioactive, posing an unnecessary health risk to personnel. As a result, a D-D plasma is used to study the physics, which can then be extrapolated to a D-T plasma in the future.

1.2 Magnetic Confinement Fusion

At temperatures on the order of KeV, this plasma cannot be confined by the walls of any container, so the plasma is confined by magnetic fields. The leading confinement scheme used today is called a "tokamak," which consists of a toroidal magnetic field produced by coils that encircle the plasma, as well as a poloidal magnetic field produced by a toroidal current generated from ohmic heating coils. This produces a helical magnetic field, and the ions and electrons spiral about the field lines. Figure 1.2 [2] shows a basic tokamak design.

A simple diagram of toroidal geometry is shown in Fig. 1.3. The poloidal field confines the plasma against drift forces, whereas the toroidal field stabilizes the plasma against pinch and kink instabilities. There is typically no radial magnetic field in a tokamak.

1.3 L-H Transition and The Edge Pedestal

After a certain amount of power has been injected into the plasma, it can transition from a low confinement mode (L-mode) to a high confinement mode (H-mode). H-mode is characterized by the outer 10% of the plasma exhibiting strong gradients in temperature and density. This edge pedestal region contains a radially inward "pinch" force. This is

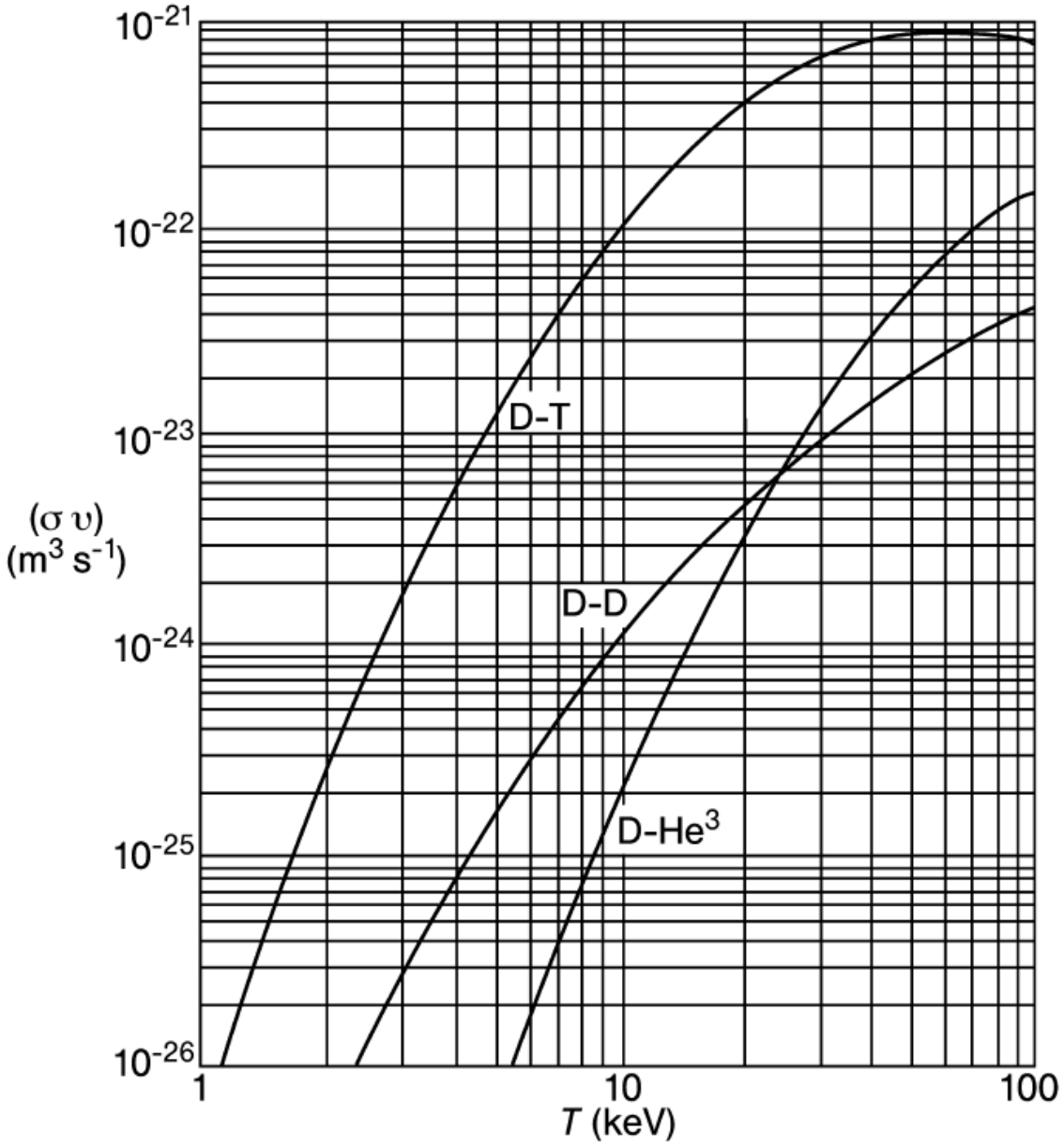

Figure 1.1: Reaction rates of interest

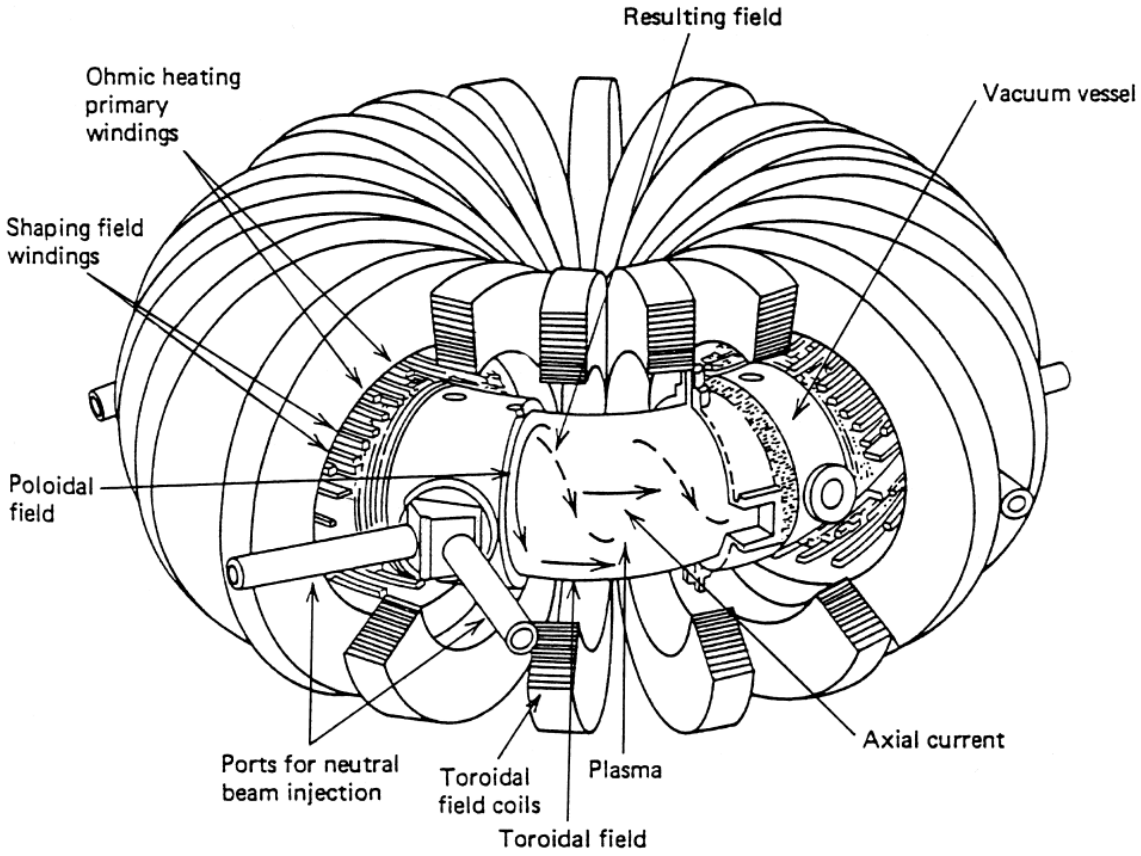

Figure 1.2: Tokamak schematic

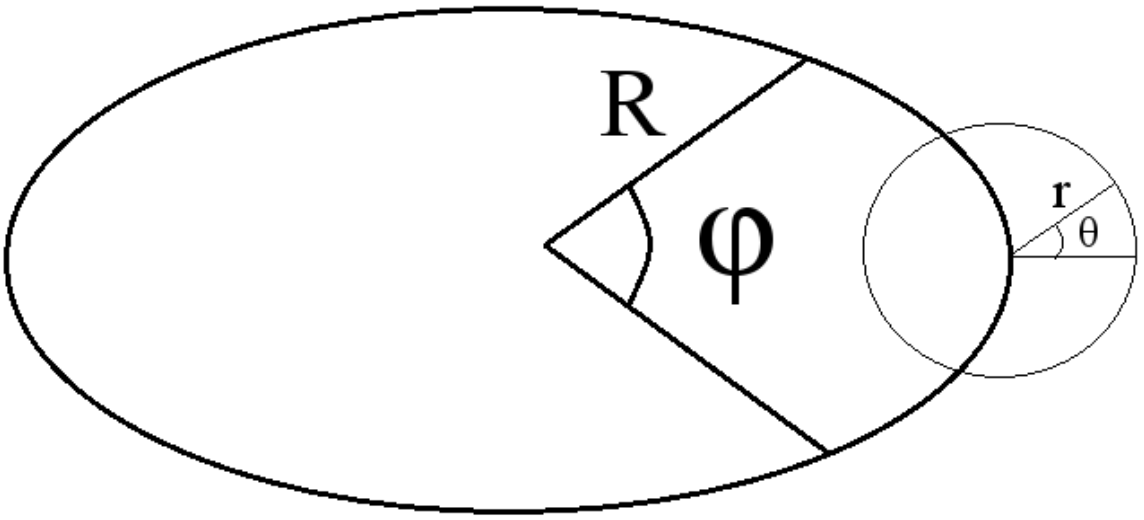

Figure 1.3: Toroidal Geometry (r, θ, ϕ)

due to primarily electromagnetic forces, which oppose the diffusive force that transports the plasma radially outward. The steep gradients that form are called the transport barrier.

The physics that controls the behavior of the edge determines the confinement of the plasma and its overall performance. The underlying physics that cause H-mode and the formation of the edge pedestal are not fully understood. As a result, the edge pedestal is a topic of intense research, especially in determining the performance of future plasmas, such as ITER.

CHAPTER 2
INTRODUCTION

Since the discovery H-mode[3], it has been associated with significantly increased energy confinement times relative to L-mode, which is a critical aspect of plasma performance. The H-mode has been observed to be associated with large gradients in plasma density, temperature, and pressure, as well as with a deep negative well in the radial electric field in the edge pedestal region. Although there are several theories regarding the cause of the formation of H-mode (e.g. Refs. [4, 5, 6, 7]), the cause of H-mode is not fully understood and remains a topic of intense research interest.

A particular interest in this thesis is the utilization of particle and momentum balance in conjunction with energy conservation to determine the different effects of two non-diffusive transport mechanisms, ion orbit loss and electromagnetic particle pinch, on particle transport in the edge for L-mode and H-mode[8, 9, 10]. The purpose of this thesis is to apply these interpretations to measurements taken from three discharges in the DIII-D tokamak[11] just before and just after the L-H transition.

A previous analysis and particle-momentum-energy balance procedure for a DIII-D discharge[12] was used to examine ion orbit loss and intrinsic rotation[12], thermal transport[13], and particle transport[14] properties during the L-H transition pedestal evolution phase of shot #118897. This analysis showed that the co-current intrinsic rotation, as well as the ion orbit loss of both particles and energy decreased significantly in the very edge of the plasma during the L-H transition, but then increased to the L-mode value in the edge approximately 20 ms after the L-H transition. In addition, the radial particle pinch changed from weakly outward in L-mode to strongly inward in H-mode. The purpose of this thesis is to extend this L-H transition investigation to include two additional DIII-D discharges, #118888 and #118890, and to repeat the analysis of #118897, but not including the evo-

lution of the H-mode pedestal. Two time slices (bins) were selected for each discharge: one in the late L-mode, and one in the early H-mode, to determine if these features are characteristic of the L-H transition in general.

CHAPTER 3

MEASUREMENT SYSTEMS AND SHOT SELECTION

3.1 DIII-D Charge Exchange Recombination (CER) Spectroscopy System

Impurity (carbon) ion temperature, density, and velocity measurements were obtained from a charge-exchange recombination (CER) spectroscopy system[15]. When the neutral beam injection (NBI) systems inject high energy, neutral deuterium atoms into the plasma, they can interact with the carbon impurities in the plasma, donating an electron and becoming ionized. The now partially ionized and excited carbon atom emits a photon when the electron de-excites to the ground state. The emitted photon can then be measured and compared with the energies that are characteristic of electron orbitals in carbon. Since the energy of the injected deuterium atoms is known, the deviation of the measured photon spectrum from the expected photon spectrum can be used to determine the density, temperature, and velocity of the carbon ions[16].

Figure 3.1 shows a plan view of the CER system. There are two sets of edge viewing chords that intersect the neutral beam lines. The point of intersection corresponds to the spatial location of the measurements for each CER chord. The tangential chords measure the toroidal velocity, and the vertical chords measure the poloidal velocity. Although this diagram shows that main ion data can be obtained from the CER system, the discharges for this work ocurred before the main ion chords were implemented, and therefore only the impurity ion properties were measured.

3.2 Thompson Scattering Diagnostics System

Electron temperature and density measurements were made with the DIII-D multipoint Thomson scattering (TS) system[18]. Lasers inject photons of a known energy into the

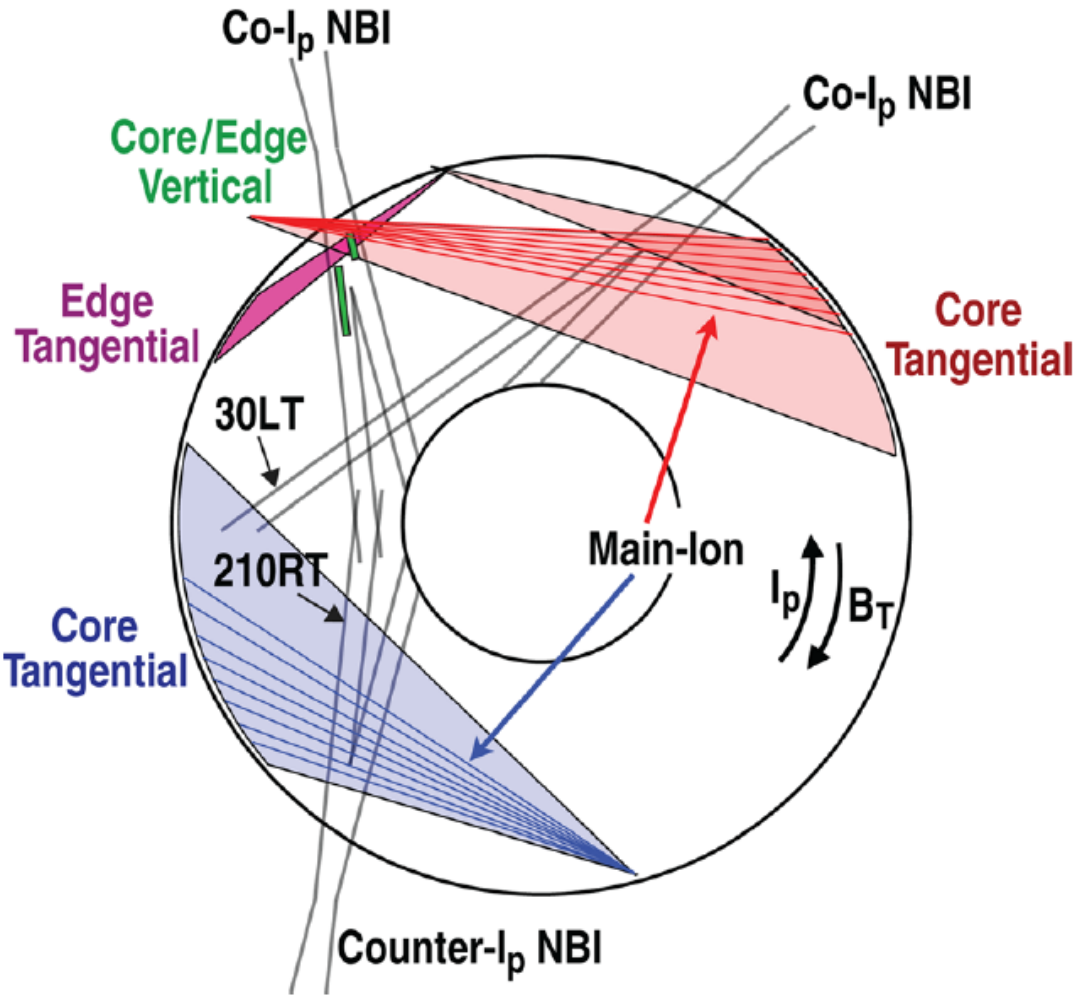

Figure 3.1: Diagram of the DIII-D CER system (Ref. [17]).

Table 3.1: Parameters of selected discharges in L-mode.

Shot #	#118897	#118888	#118890
Time Range	1510-1544 ms	1510-1544 ms	1500-1530 ms
Plasma Current	1.39 MA	1.38 MA	1.38 MA
Toroidal Field	-1.99 T	-2.00 T	-2.00 T
Major Radius R	1.71 m	1.72 m	1.71 m
Minor Radius a	0.597 m	0.598 m	0.589 m

Table 3.2: Parameters of selected discharges in H-mode.

Shot #	#118897	#118888	#118890
Time Range	1550-1569 ms	1555-1595 ms	1548-1575 ms
Plasma Current	1.39 MA	1.40 MA	1.39 MA
Toroidal Field	-2.00 T	-2.00 T	-2.00 T
Major Radius R	1.71 m	1.72 m	1.72 m
Minor Radius a	0.597 m	0.597 m	0.588 m

plasma, and they are elastically scattered by plasma electrons. The photons are then collected and their energy is measured and added to a histogram. The density of the electrons is proportional to the intensity of the scattered photons, and the thermal velocity is determined from the amount of doppler broadening observed in the expected intensity peak. The ion temperature and density are similarly measured by the CER system.

3.3 Shot Selection and Profile Fitting Procedure

Since the motivation for this thesis originated from an observation of discharge #118897[12], the two shots to be analyzed were selected from a list of discharges performed on the same day. Preference was given to shots exhibiting similar characteristics to #118897. The shots chosen were #118888 and #118890. Parameters of shots #118897, #118888, and #118890 are shown in tables 3.1 and 3.2.

An objective of this work was to obtain data with fine time resolution of plasma pa-

rameters in order to construct their time evolution across the L-H transition. This must be done whilst maintaining the quality of the data by choosing time bins such that a sufficient number of Thomson pulses and CER spectroscopy data points are included to allow an accurate average. Experimentally measured quantities include electron density, electron temperature, ion temperature, carbon density, carbon toroidal velocity, and carbon poloidal velocity.

It was determined that the optimum balance between quality of the data and time resolution was to allow for 3 Thompson pulses and CER spectroscopy data points to be included within each time bin. The data within a time bin was then averaged to produce a single data set for each measured quantity that is representative of the plasma at the given time. Time bins were selected to be just before the L-H transition (1525 ms, 1515 ms, and 1525 ms for shots #118888, #118890, and #118897, respectively) and just after the transition (1570 ms, 1560 ms, and 1555 ms for shots #118888, #118890, and #118897, respectively). All but one time bin had a time resolution under 34 ms. However, the phenomenon of interest is the decrease in carbon toroidal velocity after the L-H transition, displayed in the rightmost box of Figs. 3.2, 3.3, and 3.4. One can see that the velocity decreases after the L-H transition, but then recovers in < 34 ms, which is included in the time averaging of the H-mode time-slice, reducing the magnitude of this observation. The L-mode time bin for shot #118888 was extended to 154 ms to avoid errors in the fitting algorithm. The profiles show little variation over this time range, so this procedure is not considered a problem for the L-mode analysis. Also, macroscopic parameters such as major radius, minor radius, neutral beam injection (NBI) power, etc. did not require fitting, and were therefore measured with a much smaller time bin (< 34 ms).

The data fitting procedure involved using a spline-fitted[19] pedestal profile of the carbon ion properties, and hyperbolic tangent fits[20] of the electron properties. The spline-fitted profiles were automatically generated and manually tuned using spline knots. After the profile fits were determined not to have superfluous structure, the ONETWO[21]

code was run to calculate the heating and rotational effects of neutral beams on ions and electrons, such as contributing to the source terms for fast and thermal ions, ion toroidal momentum, and ion and electron energy.

Specialized scripts were used to calculate and extract data from the DIII-D MDSPlus database at twenty-five radial locations in the edge plasma, ranging from $\rho = 0.864$ to $\rho = 1.0$. The variables of interest include all properties previously mentioned as well as their gradient scale lengths and time derivatives. They were then used as inputs in the GTEDGE[22, 23] code for analysis.

Figures 3.2, 3.3, and 3.4 show the time dependent toroidal velocity from one CER chord in the edge, and the D_α signal for each shot. The boxed areas are the time slices for the L and H modes, respectively. The D_α signal was used to determine the time of the L-H transition. The CER chords remain stationary, so their location relative to the separatrix varies depending on the discharge and time. The location of the separatrix is determined from the radial electron temperature profile, and therefore also varies. The CER chords shown in Figs. 3.2-3.4 are located at $\rho \approx 0.98$. Time dependent measurements of the injected neutral beam power and the pedestal electron density and temperature can be found in Appendix A. Radial profiles of densities and temperatures are found in the next section.

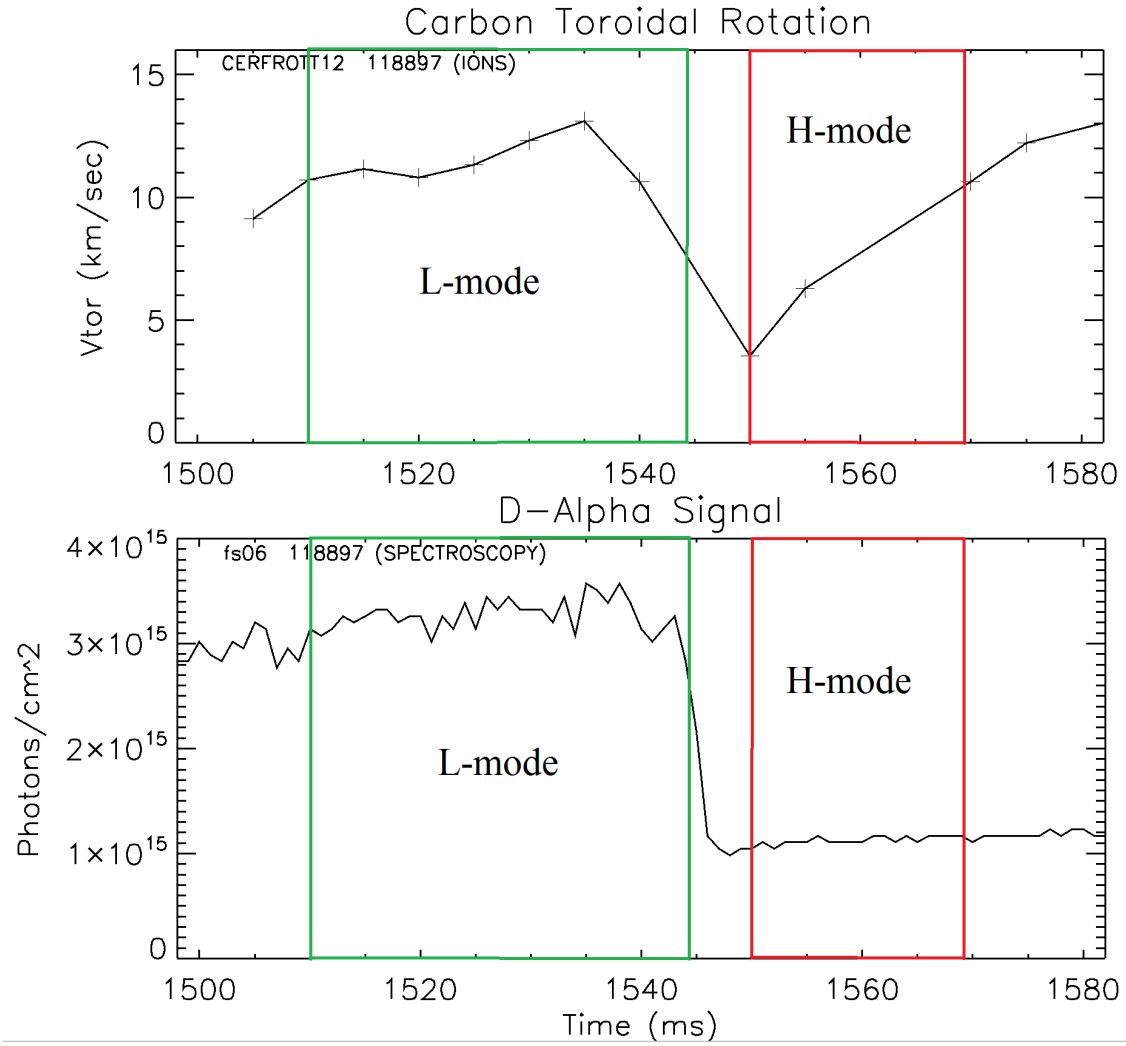

Figure 3.2: Time dependent experimental data for shot #118897. The upper panel is the toroidal rotation at $\rho \approx 0.98$ and the lower panel is the D_α signal from the lower divertor. The leftmost box is the L-mode time-slice, and the rightmost box is the H-mode time-slice

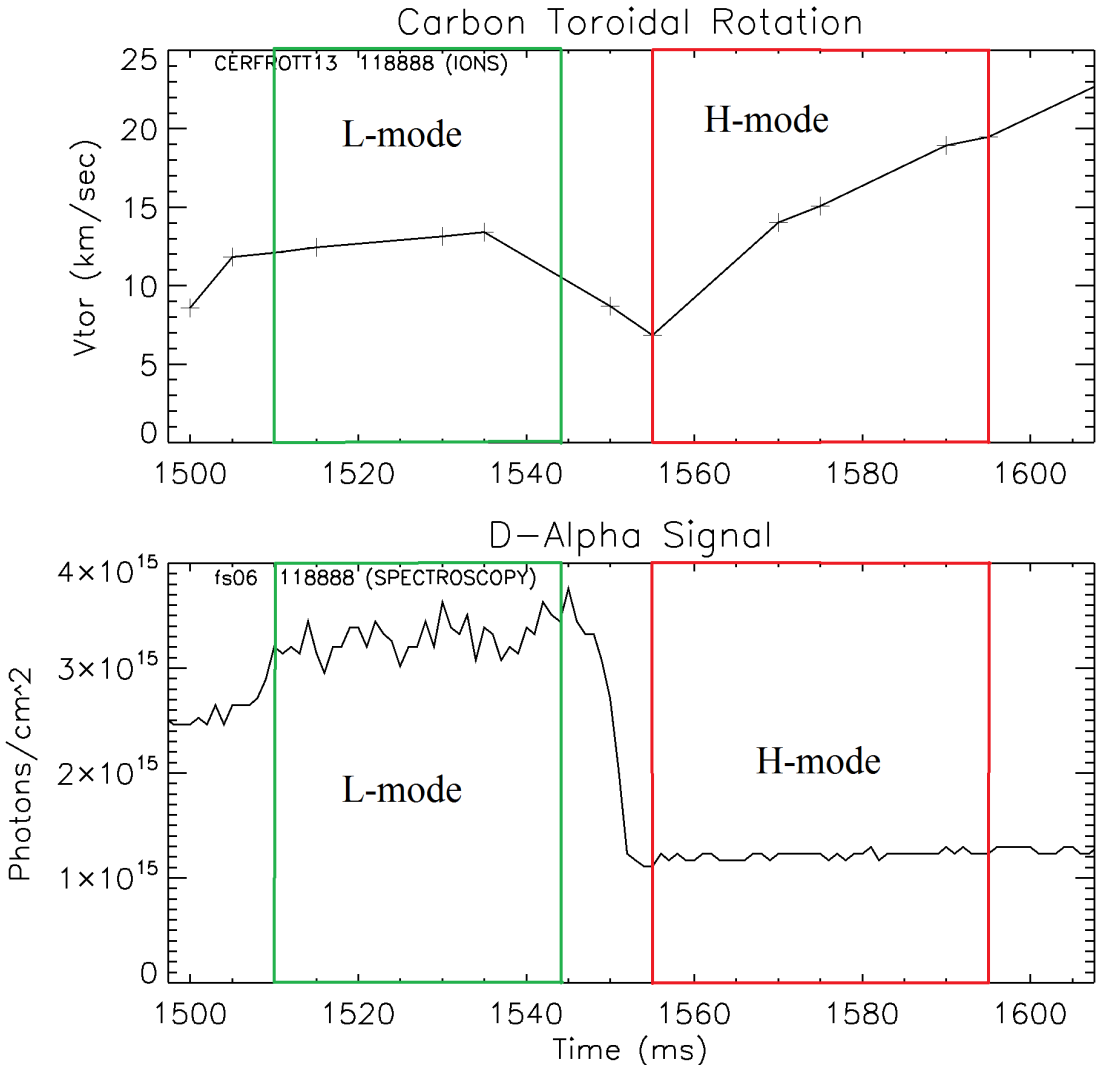

Figure 3.3: Time dependent experimental data for shot #118888. The upper panel is the toroidal rotation at $\rho \approx 0.98$ and the lower panel is the D_α signal from the lower divertor. The leftmost box is the L-mode time-slice, and the rightmost box is the H-mode time-slice

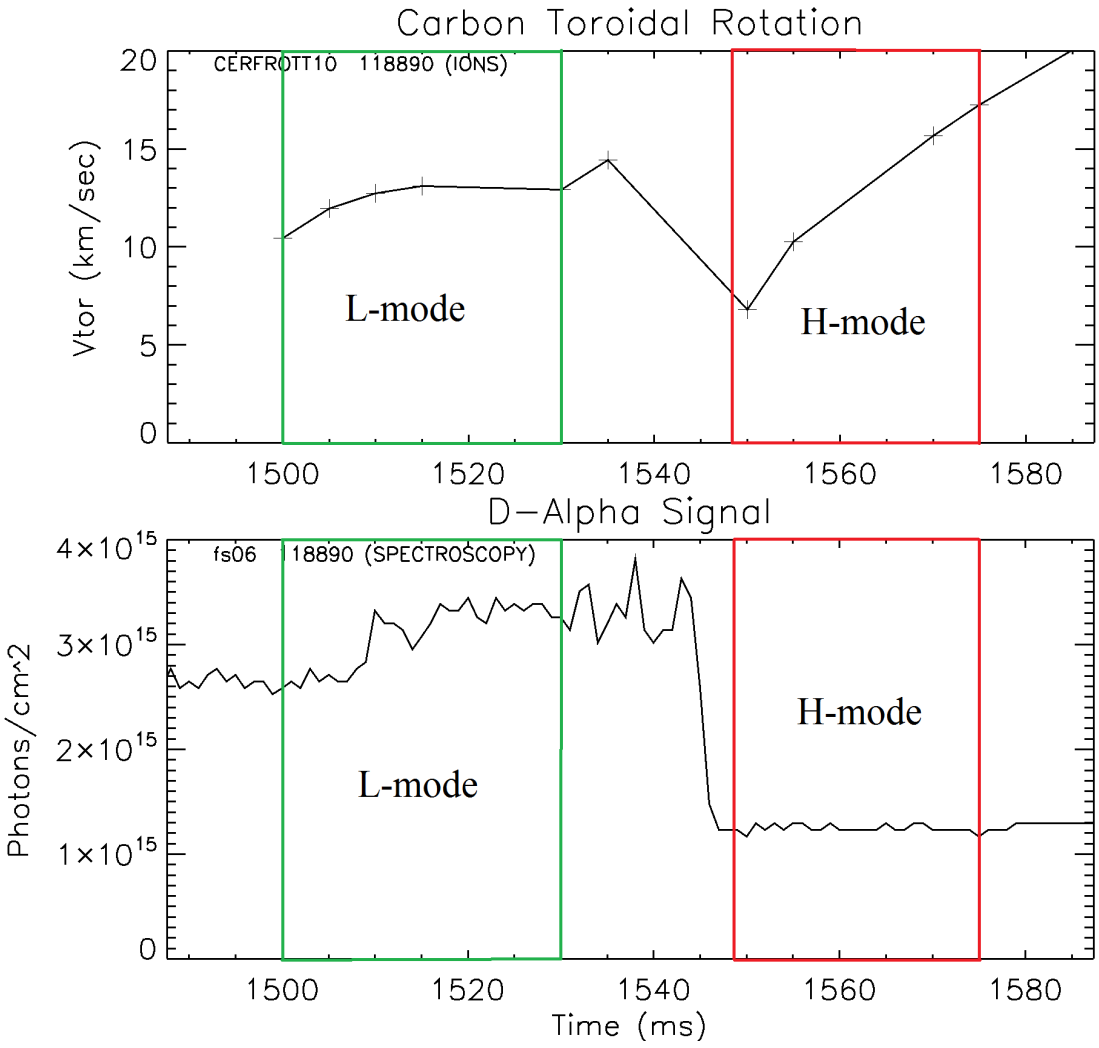

Figure 3.4: Time dependent experimental data for shot #118890. The upper panel is the toroidal rotation at $\rho \approx 0.98$ and the lower panel is the D_α signal from the lower divertor. The leftmost box is the L-mode time-slice, and the rightmost box is the H-mode time-slice

CHAPTER 4

GTEDGE BACKGROUND PLASMA

A "background" plasma must be modeled in order to obtain particle and heat fluxes crossing the separatrix outward into the scrape-off-layer (SOL), neutral particle fluxes crossing the separatrix inward to fuel the core plasma, and the distribution of neutral particles in the plasma edge. This is necessary to develop particle and energy boundary conditions for the core and edge of the plasma.

This background plasma is modeled using the interpretive code, GTEDGE[22, 23], which inputs experimental data from the DIII-D MDSPlus database. GTEDGE calculates recycling neutral particle densities and reaction rates in the plasma by utilizing a simple 2-D coupled core-plasma-divertor/SOL-plasma-recycling/fueling-neutrals calculation. Power and particle balances are solved in the core to determine power and particle fluxes into the SOL. A 2-point model is used to solve for the plasma density and temperature at the divertor plate and at the plasma outboard midplane. Recycling neutrals from the divertor are input to a 2D neutral transport calculation (including charge-exchange neutral fluxes to the wall and recycling neutrals from the divertor) to calculate the neutral flux inward across the separatrix in the vicinity of the x-point and at the outboard midplane. A 1D neutrals calculation attenuates the neutral flux into the plasma at these locations. Geometric and operating parameters such as major and minor radius, plasma elongation and triangularity, location of the x-point, magnetic field, plasma current, and strike point locations are used to model the plasma and divertor regions.

GTEDGE approximates the elongated plasma as a circular plasma with elongation factor κ and an effective minor radius $\bar{r} = r\sqrt{(1+\kappa)^2/2}$ which conserves flux surface area. The approximate circular representation of the magnetic flux surface geometry is described by

$$R(r,\theta) = \bar{R}h(r,\theta), B_{\theta,\phi}(r,\theta) = \bar{B}_{\theta,\phi}/h(r,\theta),$$
$$h(r,\theta) = (1 + (r/\bar{R})cos\theta). \tag{4.1}$$

From the assumption of uniform current density, Ampere's Law gives for the poloidal magnetic flux enclosed by the flux surface at radius $\rho \equiv \bar{r}/\bar{a}$

$$\Psi(\rho) = RA_\phi = \frac{1}{2}\left(\frac{\mu_0 I}{2\pi a^2}\right)\bar{R}\bar{a}^2\rho^2. \tag{4.2}$$

CHAPTER 5

EXPERIMENTAL DATA

5.1 Density and Temperature

The electron density and temperature were measured with the Thomson scattering system[18]. The tanh fitted electron density profiles displayed in Fig. 5.1 all show pedestal formation following the L-H transition. The electron density edge pedestal location (the point at which the profile changes from a flat top region to a steep gradient region) is about $\rho = 0.98$ for shots #118897 and #118890, and $\rho = 0.96$ for shot #118888. However, the edge pedestal location for electron temperature (shown in Fig. 5.2) is $\rho \sim 0.95$ for all three discharges.

The ion temperatures shown in Fig. 5.3 were measured with the CER system[15] and fitted using a b-spline[19]. After the L-H transition, an increase in ion temperature throughout the entire edge region is observed for all 3 shots. There is, however, little discernible formation of separate flat top and steep gradient regions in the ion temperature just after the L-H transition.

5.2 Velocity and Radial Electric Field Profiles

The experimental toroidal and poloidal rotation velocities were obtained using an edge CER system of tangentially and vertically viewing chords[15]. These were measured for C^{6+} impurity and then fit with a b-spline[19].

In L-mode, the toroidal rotation profile shown in Fig. 5.4 is relatively flat across the entire edge region ($\rho > 0.85$) for all shots. The toroidal rotation for discharge #118897 is greater in H-mode than in L-mode for $\rho < 0.95$, but drops significantly below its L-mode value for $0.95 < \rho < 1$, forming a well centered about $\rho = 0.97$. For discharge #118888

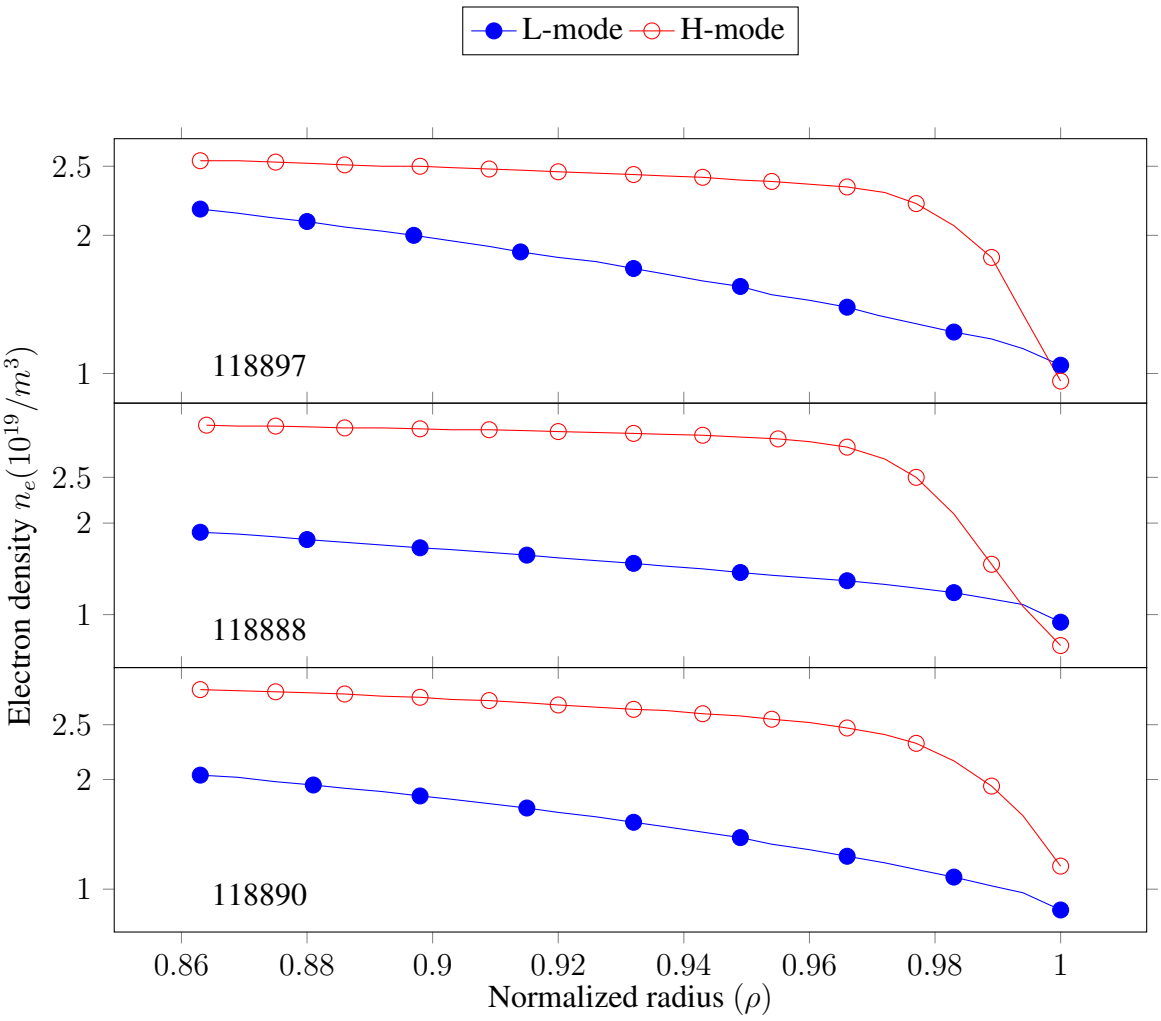

Figure 5.1: Fitted experimental electron density profiles

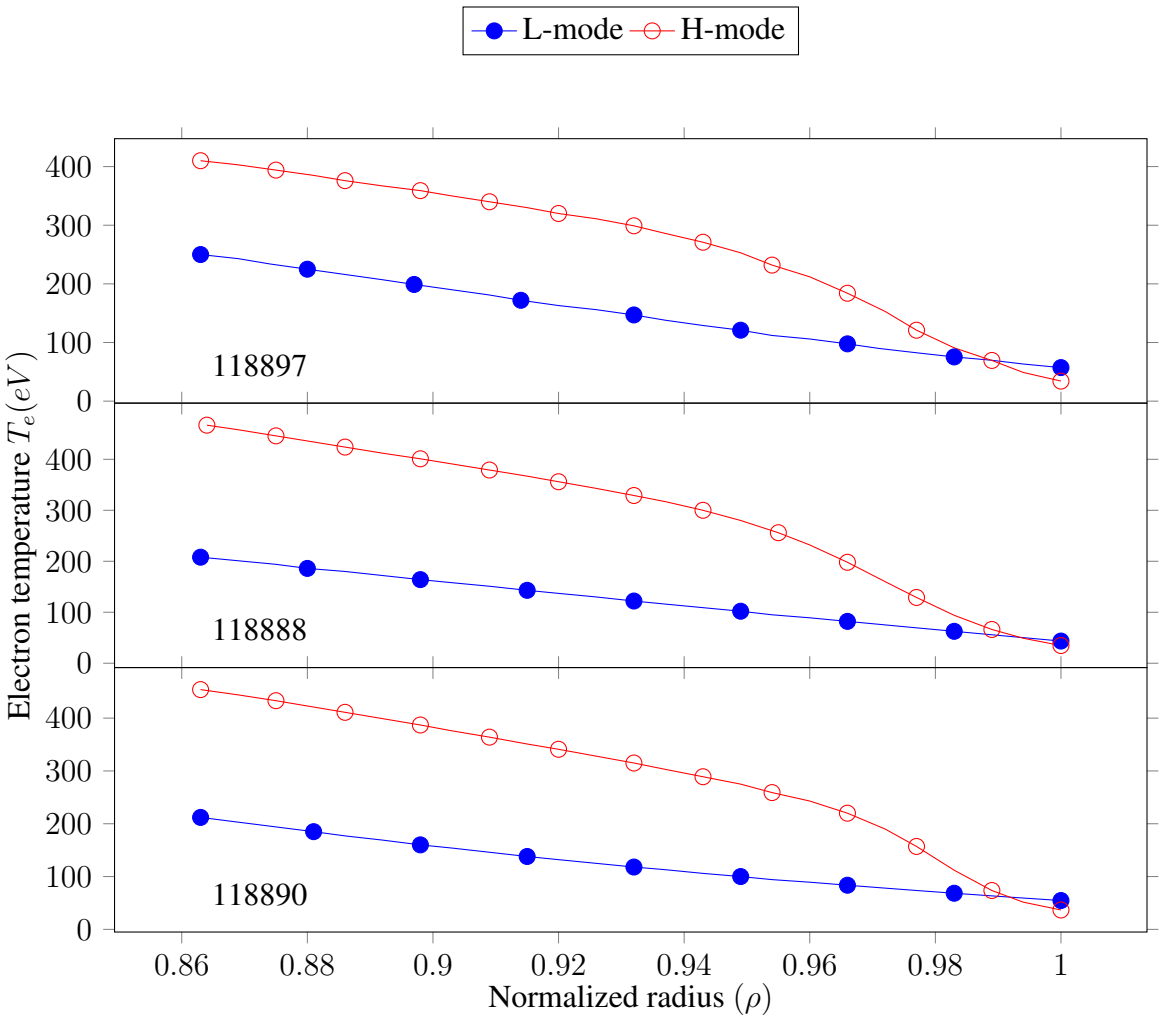

Figure 5.2: Fitted experimental electron temperature profiles

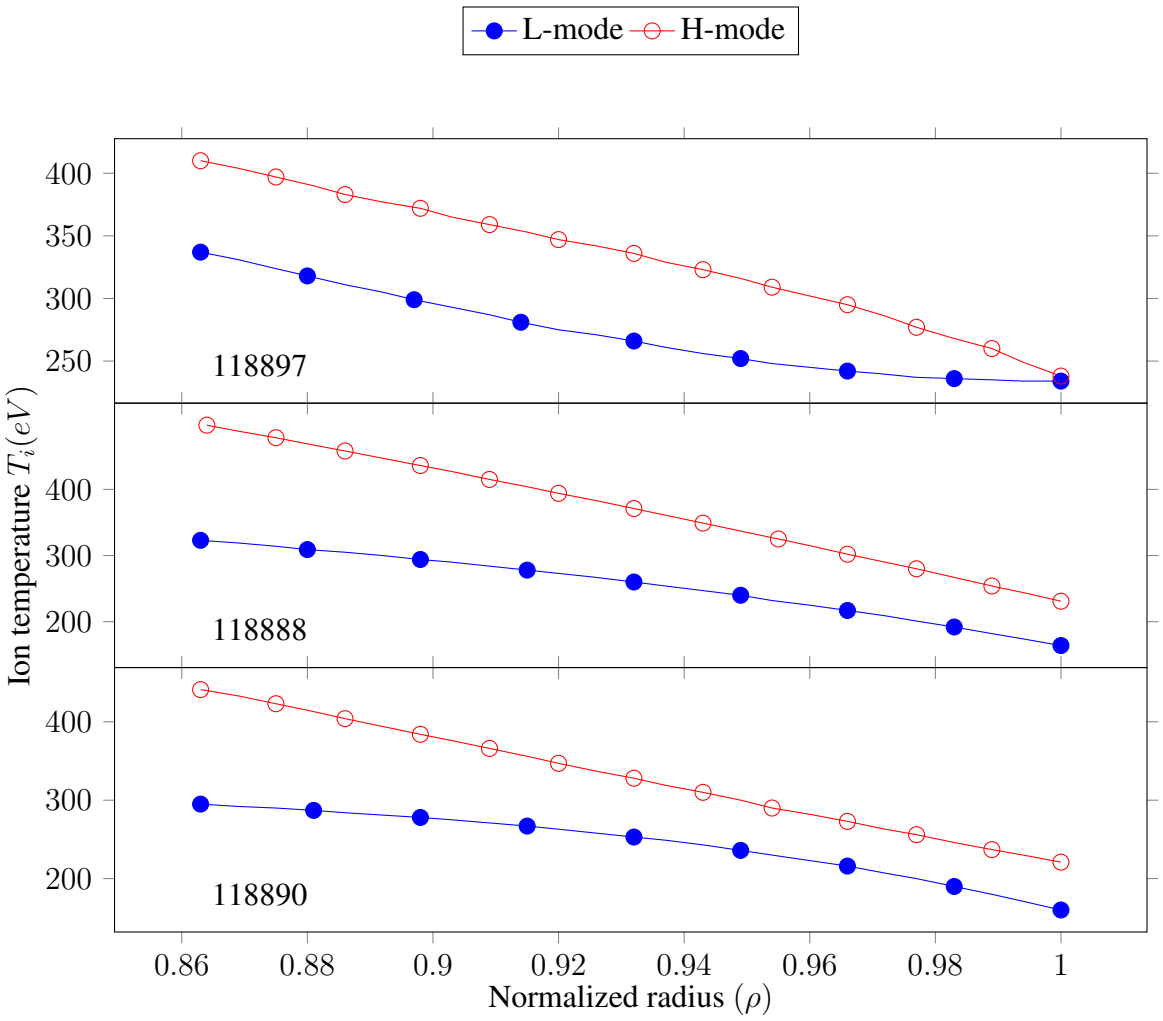

Figure 5.3: Fitted experimental ion temperature profiles

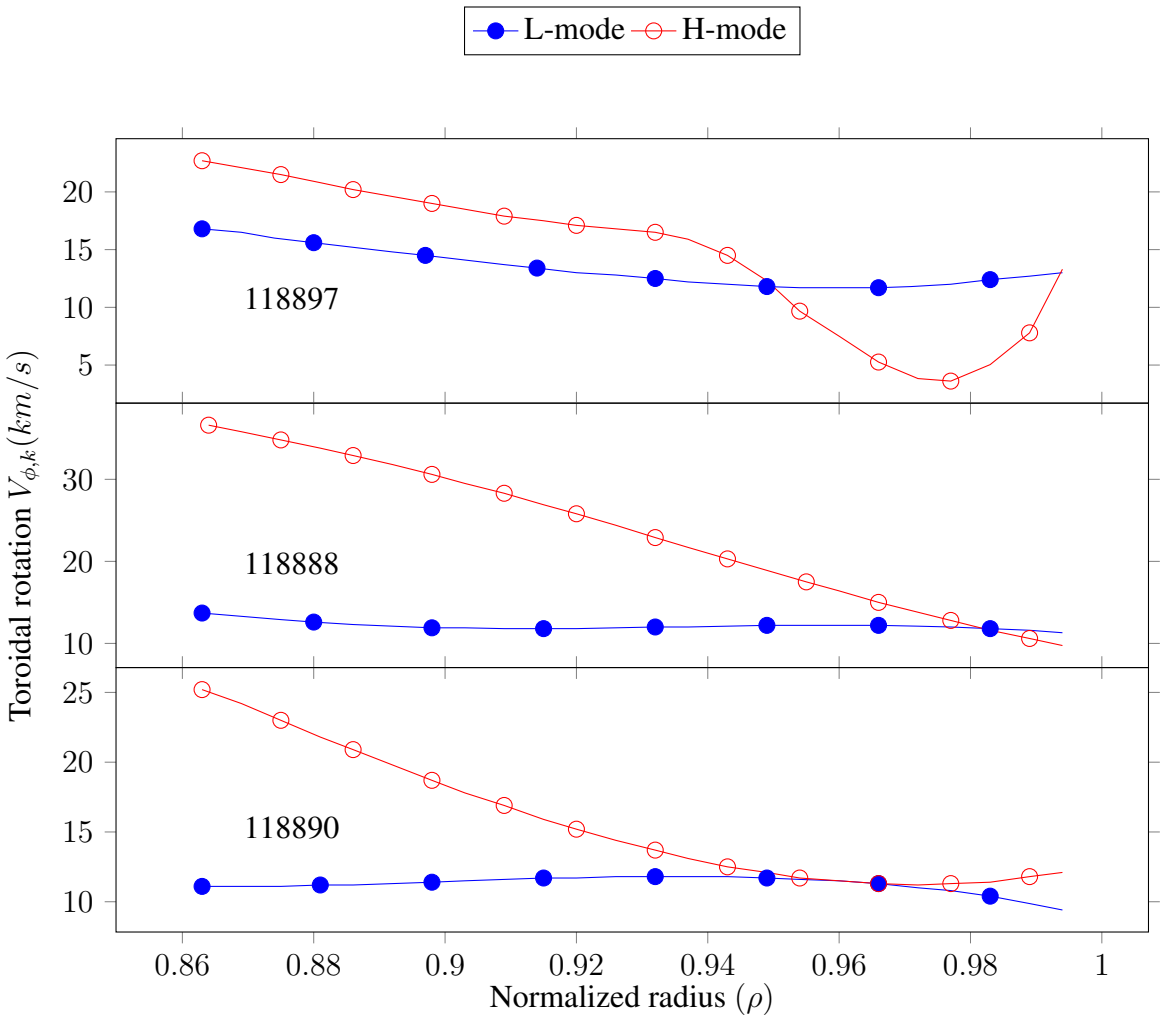

Figure 5.4: Fitted experimental carbon toroidal rotation profiles

the toroidal rotation is greater in H-mode than in L-mode throughout the edge region, but decreases linearly with radius and drops just below its L-mode value at $\rho = 0.99$. For $\rho > 0.95$ in discharge #118890, the H-mode toroidal velocity only slightly increases above its L-mode value. The decrease in the carbon toroidal rotation in the edge after the L-H transition is not consistent across discharges, but this may be due to a comparatively coarse time resolution. Figures 3.2-3.4 explicitly show a decrease in the carbon toroidal rotation at $\rho \approx 0.98$, and a significant increase 10 ms later, for all three shots. The transient decrease and increase in toroidal rotation is measured and averaged over the time-slice to generate the radial profile of toroidal velocity. The time averaging of rotation data washes out the effect of decreasing carbon toroidal rotation in the edge after the L-H transition. Nevertheless, we aim to test the hypothesis that a reduction in ion orbit loss in the edge after the L-H transition causes the transient drop in toroidal rotation after the L-H transition shown in Figs. 3.2-3.4.

The carbon poloidal rotation velocity profiles shown in Fig. 5.5 exhibit somewhat similar structure to those of the toroidal rotation. The L-mode poloidal rotation profiles are more or less flat and positive throughout the edge region. In all 3 cases, the H-mode poloidal rotation decreases below its L-mode value for $\rho < 0.92$. Discharges #118888 and #118890 develop a well-like structure at $\rho \approx 0.97$. The variation in profile shapes may be partially related to averaging effects during the analysis procedure. (In this paper the sign convention regarding toroidal geometry follows the right hand rule convention. The direction of the current (counter-clockwise looking down) is taken to be the positive toroidal direction. Therefore, the positive poloidal direction is downward on the outboard midplane.)

The radial electric field is a quantity that can be inferred from a radial momentum balance on carbon ions (indicated by subscript "k"), using the measured C^{6+} impurity density, temperature, and rotation velocities. The radial force balance equation is:

$$E_r = \frac{1}{n_k e_k}\frac{\partial p_k}{\partial r} - (V_{\theta,k}B_\phi - V_{\phi,k}B_\theta) \tag{5.1}$$

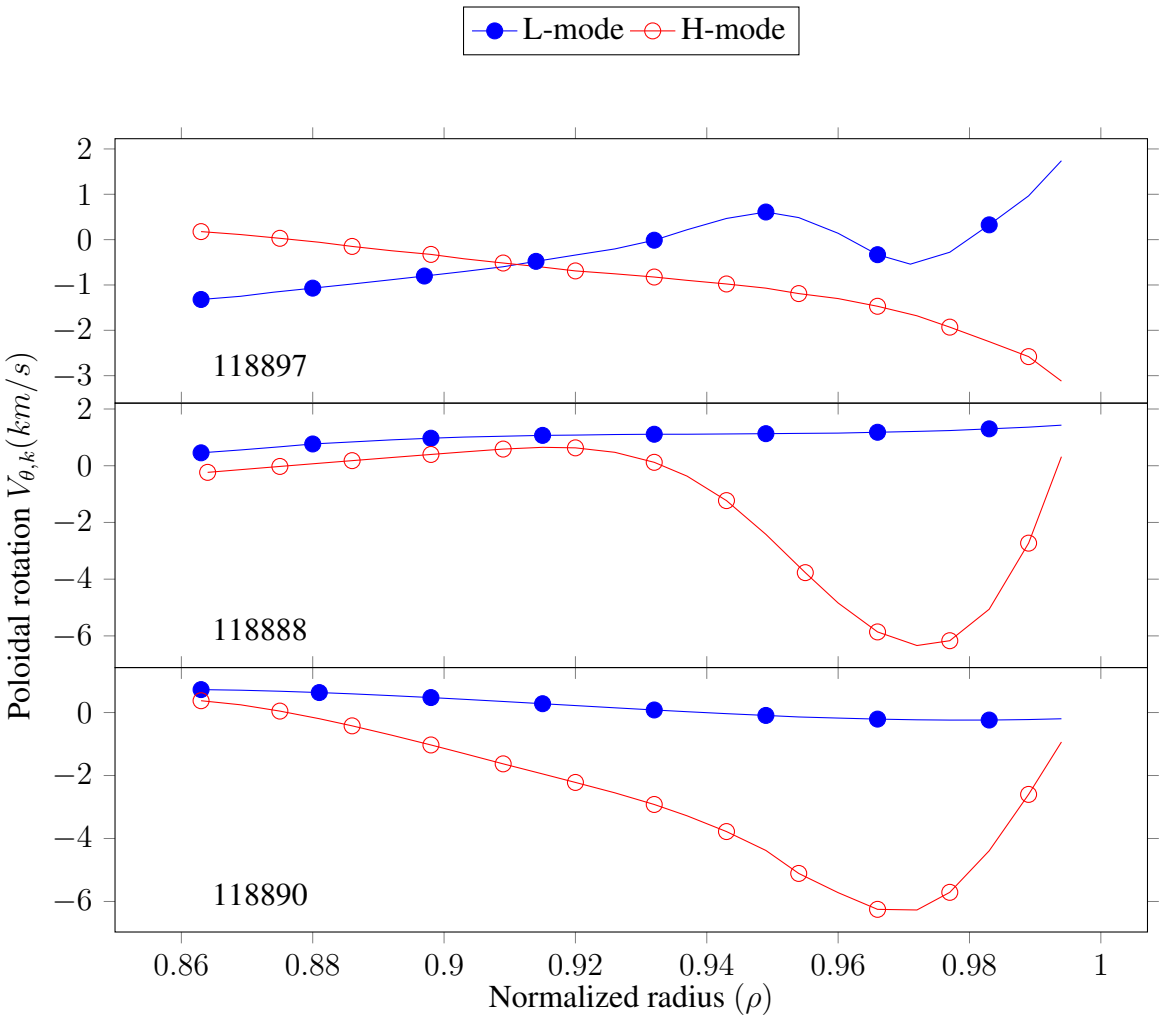

Figure 5.5: Fitted carbon poloidal rotation profiles

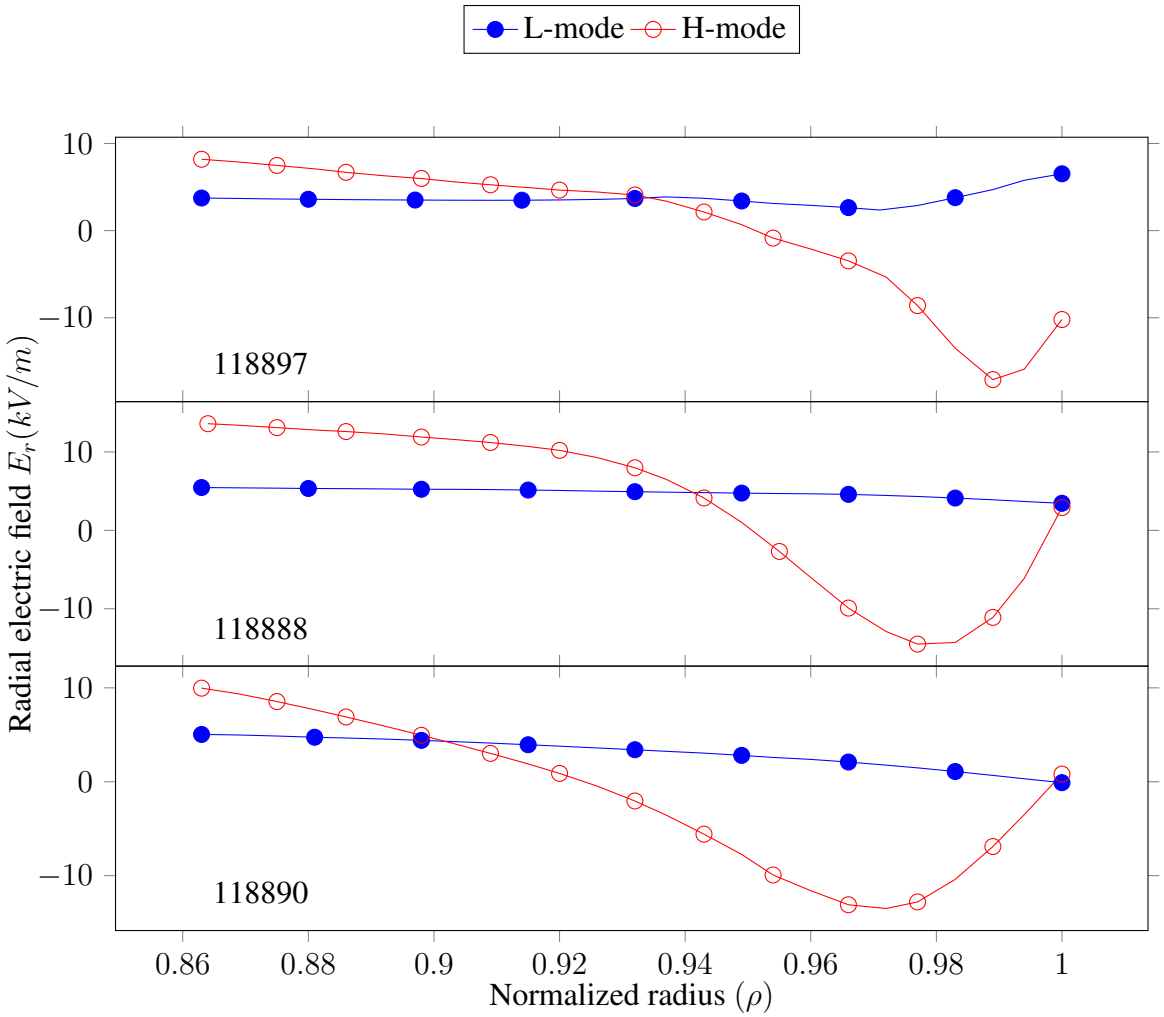

Figure 5.6: Experimental radial electric field calculated from carbon radial momentum balance

In all 3 discharges, the radial electric field of Eq. (5.1) evaluated for C^{+6} and displayed in Fig. 5.6, remains positive and relatively flat throughout the edge region in L-mode. Just after the L-H transition, the radial electric field becomes negative in the outer edge and forms a well-like structure. The well depth is about the same for all three discharges, but the location varies by a few mm.

CHAPTER 6

PARTICLE AND MOMENTUM TRANSPORT IN THE EDGE PEDESTAL

6.1 Ion Orbit Loss

Thermalized ions flowing slowly radially outward can access loss orbits which will carry them quickly across the separatrix. For an ion with a given direction at a given point on an internal flux surface Ψ_0, the minimum energy for the kinetic loss across the separatrix at a point Ψ_s can be calculated from the requirement for conservation of canonical angular momentum, energy, and magnetic moment[24, 25, 26].

The conservation of canonical toroidal angular momentum[24, 27] for an ion introduced at point "0" on an internal flux surface and traveling to point "S" on the separatrix is

$$R_s m V_{\parallel,s} f_{\phi,s} + e\Psi_s = const = R_0 m V_{\parallel,0} f_{\phi,0} + e\Psi_0 \tag{6.1}$$

where $V_\parallel$ is the parallel velocity, $f_\phi = \frac{B_\phi}{|B|}$, R is the major radius, and Ψ is the flux surface value. Combining the conservation of energy and of magnetic moment

$$\begin{aligned} \frac{1}{2}m(V_{\parallel,s}^2 + V_{\perp,s}^2) + e\phi_s = const &= \frac{1}{2}m(V_{\parallel,0}^2 + V_{\perp,0}^2) + e\phi_0 \\ &\equiv \frac{1}{2}mV_0^2 + e\phi_0 \end{aligned} \tag{6.2}$$

$$\frac{mV_{\perp,s}^2}{2B_s} = const = \frac{mV_{\perp,0}^2}{2B_0} \tag{6.3}$$

yields

$$V_{\parallel,s} = \pm V_0 \left[1 - \left| \frac{B}{B_0} \right| (1 - \zeta_0^2) + \frac{2e}{mV_0^2}(\phi_0 - \phi_s) \right]^{\frac{1}{2}} \tag{6.4}$$

where ϕ is the electrostatic potential, which is derived from the measured radial electric field, and ζ_0 is the cosine of the initial guiding center velocity relative to the toroidal magnetic field. Substituting Eq. (6.4) into Eq. (6.1) results in a quadratic equation

$$\begin{aligned} V_0^2 \left[\left(\left| \frac{B_s}{B_0} \right| \frac{f_{\phi,0}}{f_{\phi,s}} \zeta_0 \right)^2 - 1 + (1 - \zeta_0^2) \left| \frac{B_s}{B_0} \right| \right] + \\ V_0 \left[\frac{2e(\Psi_0 - \Psi s)}{R_s m f_{\phi,s}} \left(\left| \frac{B_S}{B_0} \right| \frac{f_{\phi,0}}{f_{\phi,s}} \zeta_0 \right) \right] + \\ \left[\left(\frac{e(\Psi_0 - \Psi_s)}{R_s m f_{\phi,s}} \right)^2 - \frac{2e(\phi_0 - \phi_s)}{m} \right] = 0 \end{aligned} \tag{6.5}$$

for the minimum escape speed $V_0 = V_{0,min}$ for a particle with initial poloidal location θ_0 on an internal flux surface with initial direction cosine (relative to the toroidal B_ϕ) ζ_0 to escape across the separatrix at a poloidal location θ_s, provided that location "S" is chosen to be on the last closed flux surface (LCFS). Note that since the particle species enters Eq. (6.5) as e/m, $V_{0,min}$ is the same for deuterium $(e/m = 1/2 = const)$ and for carbon $(e/m = 6/12 = 1/2 = const)$, but the minimum energy $E_{min} = \frac{1}{2} m V_{0,min}^2$, is not the same for carbon and deuterium.

This equation is solved on 24 internal flux surfaces, on each for 8 poloidal locations and for 22 different initial direction cosines ζ_0, and for 8 poloidal exit locations on the LCFS. All ions with energy greater than $E_{min} = \frac{1}{2} m V_{0,min}^2$ (corresponding to speed $V_{0,min}$) are assumed to cross the LCFS. Half of these ions that are IOL out of the plasma are estimated to exist on orbits that allow them to return to the plasma ($R_{loss} = 0.5$) without interacting within the scrape off layer (SOL)[25] or striking the wall. Further details on how GTEDGE distributes ion loss locations is covered in detail in Ref. [26].

Ions that travel in the direction opposite to the plasma current generally have a signifi-

cantly smaller $V_{0,min}$ (are lost at lower energies) than ions at the same location with velocity parallel to the plasma current. This is due to the fact that counter-current ions execute banana orbits that result in an outward radial excursion from the flux surface. This behavior is most extreme when an ion is traveling antiparallel ($\zeta_0 = 1$ with B_ϕ and I_ϕ oppositely directed, as with the shots analyzed in this paper) to the current, and decreases in severity as ζ_0 decreases. Figure 6.1 shows the lowest minimum energy for loss, $E_{min}(\zeta_0, \rho_0)$, for any θ_0 on two internal flux surfaces (note that the plasma current and toroidal magnetic field are oppositely directed in these shots). The minimum energy for ion orbit loss from an internal flux surface is somewhat lower in L-mode than in H-mode.

For all 3 discharges the minimum loss energy for ions is greater in H-mode than in L-mode. This, combined with the observation that the ion temperature in the edge only slightly increases after the L-H transition as shown in Fig. 5.3, results in a calculated reduction of IOL at the L-H transition. The difference between the minimum loss energies of L-mode and H-mode in the ctr-current direction $\zeta_0 > 0$ is greater than in the co-current direction $\zeta_0 < 0$. For all direction cosines in the very edge $(\rho > 0.972), E_{min}$ is approximately an order of magnitude smaller than at $\rho = 0.887$. E_{min} falls within the distribution of thermalized ions in the edge plasma, indicating that some ions are ion orbit lost.

Since $V_{0,min}$ decreases with radius, cumulative loss fractions can be defined that increase with radius for the outflowing plasma ions. The cumulative loss fractions are F_{orb} for particles, M_{orb} for momentum, and E_{orb} for energy, in which

$$\begin{aligned} F_{orb}(\rho) \equiv \frac{N_{loss}}{N_{tot}} &= \frac{\int_{-1}^{1} d\zeta_0 \int_{V_{0,min}(\rho_0,\zeta_0)}^{\infty} f(V_0) V_0^2 dV_0}{\int_{-1}^{1} d\zeta_0 \int_{0}^{\infty} f(V_0) V_0^2 dV_0} \\ &= \frac{\int_{-1}^{1} d\zeta_0 \int_{\epsilon_{min}(\rho_0,\zeta_0)}^{\infty} \epsilon^{1/2} e^{-\epsilon} d\epsilon}{\int_{-1}^{1} d\zeta_0 \int_{0}^{\infty} \epsilon^{1/2} e^{-\epsilon} d\epsilon} \\ &= \frac{\int_{-1}^{1} \Gamma(\frac{3}{2}, \epsilon_{min}(\rho_0, \zeta_0)) d\zeta_0}{2\Gamma(\frac{3}{2})} \end{aligned} \tag{6.6}$$

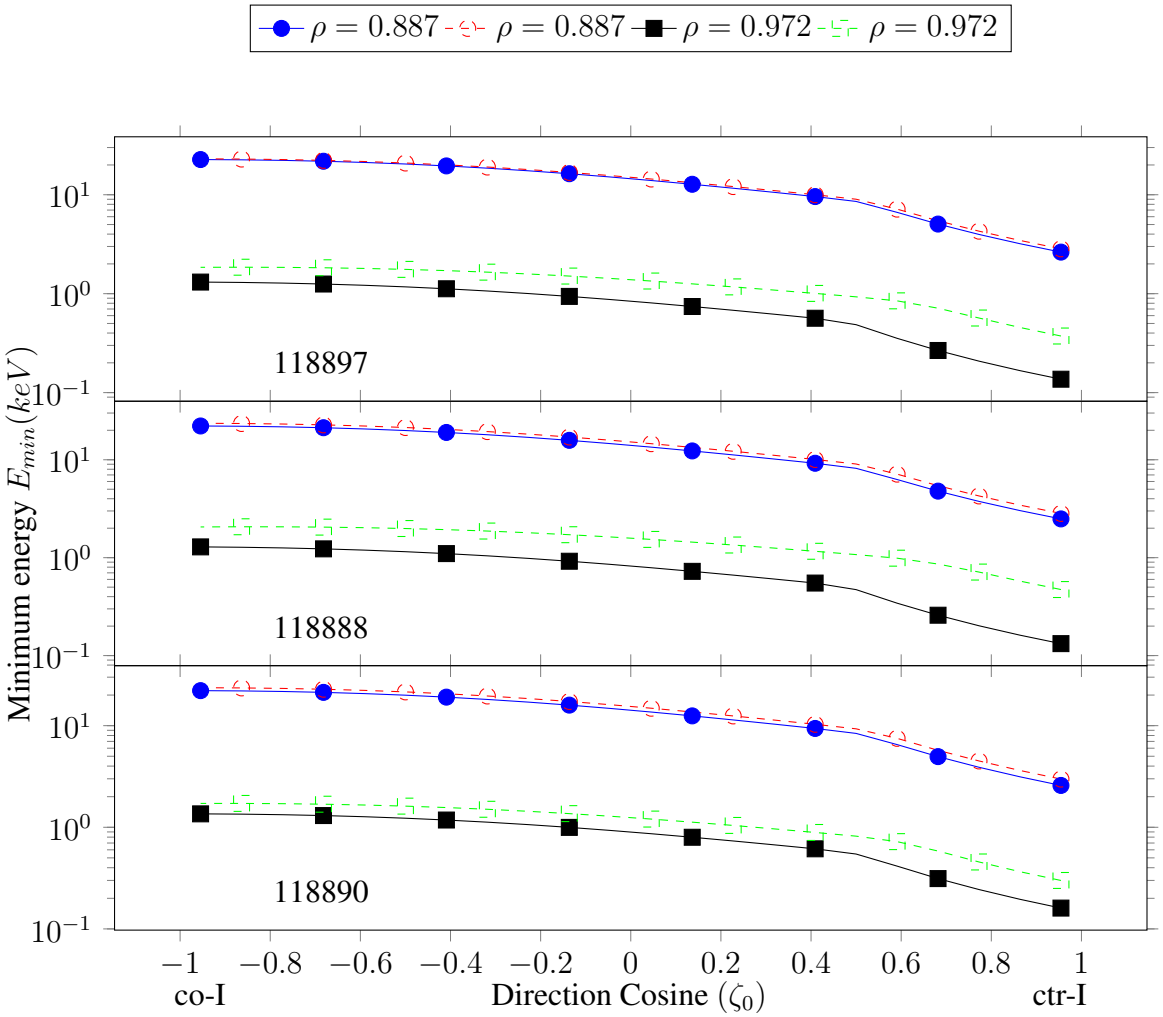

Figure 6.1: Lowest $E_{min}(\zeta_0, \rho_0)$ for deuterium for all uniformly distributed launch locations θ_0 on two internal flux surfaces (solid symbols for L-mode and empty symbols for H-mode)

$$M_{orb}(\rho_0) \equiv \frac{M_{loss}}{M_{tot}} = \frac{\int_{-1}^{1} \zeta_0 d\zeta_0 \int_{V_{0,min}(\rho_0,\zeta_0)}^{\infty} (mV_0) f(V_0) V_0^2 dV_0}{\int_{-1}^{1} d\zeta_0 \int_0^{\infty} (mV_0) f(V_0) V_0^2 dV_0}$$
$$= \frac{\int_{-1}^{1} \zeta_0 \Gamma(2, \epsilon_{min}(\rho_0, \zeta_0)) d\zeta_0}{2\Gamma(2)} \tag{6.7}$$

$$E_{orb}(\rho_0) \equiv \frac{E_{loss}}{E_{tot}} = \frac{\int_{-1}^{1} d\zeta_0 \int_{V_{0,min}(\rho_0,\zeta_0)}^{\infty} (\frac{1}{2} mV_0^2) f(V_0) V_0^2 dV_0}{\int_{-1}^{1} d\zeta_0 \int_0^{\infty} (\frac{1}{2} mV_0^2) f(V_0) V_0^2 dV_0}$$
$$= \frac{\int_{-1}^{1} \Gamma(\frac{5}{2}, \epsilon_{min}(\rho_0, \zeta_0)) d\zeta_0}{2\Gamma(\frac{5}{2})} \tag{6.8}$$

where $\epsilon_{min}(\rho_0, \zeta_0) \equiv E_{min}(\rho_0, \zeta_0)/kT_{ion}(\rho_0) \equiv mV_{0,min}^2(\rho_0, \zeta_0)/2kT_{ion}(\rho_0)$ is the reduced energy corresponding to the minimum velocity for which ion orbit loss is possible. $\Gamma(n)$ is the complete gamma function of order n, and $\Gamma(n, x) = \Gamma(n) - \gamma(n, x)$, where $\gamma(n, x)$ is the incomplete gamma function of order n and argument x. An initially Maxwellian ion distribution, but chopped off above $V_{0,min}$, has been assumed for the purpose of evaluating these velocity integrals.

Figures 6.2 and 6.3 show semi-log plots of the cumulative particle and energy loss fractions for all three discharges. After the L-H transition, the particle loss fraction increases slightly for $\rho < 0.95$ due to the increase in ion temperature and radial electric field in H-mode relative to L-mode, allowing for more ions to be lost. However, there is a decrease from L-mode to H-mode in cumulative ion particle and energy loss for $\rho > 0.95$. Figure 6.1 shows that for $\rho = 0.887$, E_{min} is almost the same for L-mode and H-mode, but for $\rho = 0.972$ E_{min} is significantly greater in H-mode than in L-mode. This explains why the cumulative loss fractions show a slight increase for $\rho < 0.95$, but decrease for $\rho > 0.95$ after the L-H transition. For discharge #118890 the particle and energy loss fractions decrease only slightly in the far edge for H-mode relative to L-mode, and are approximately

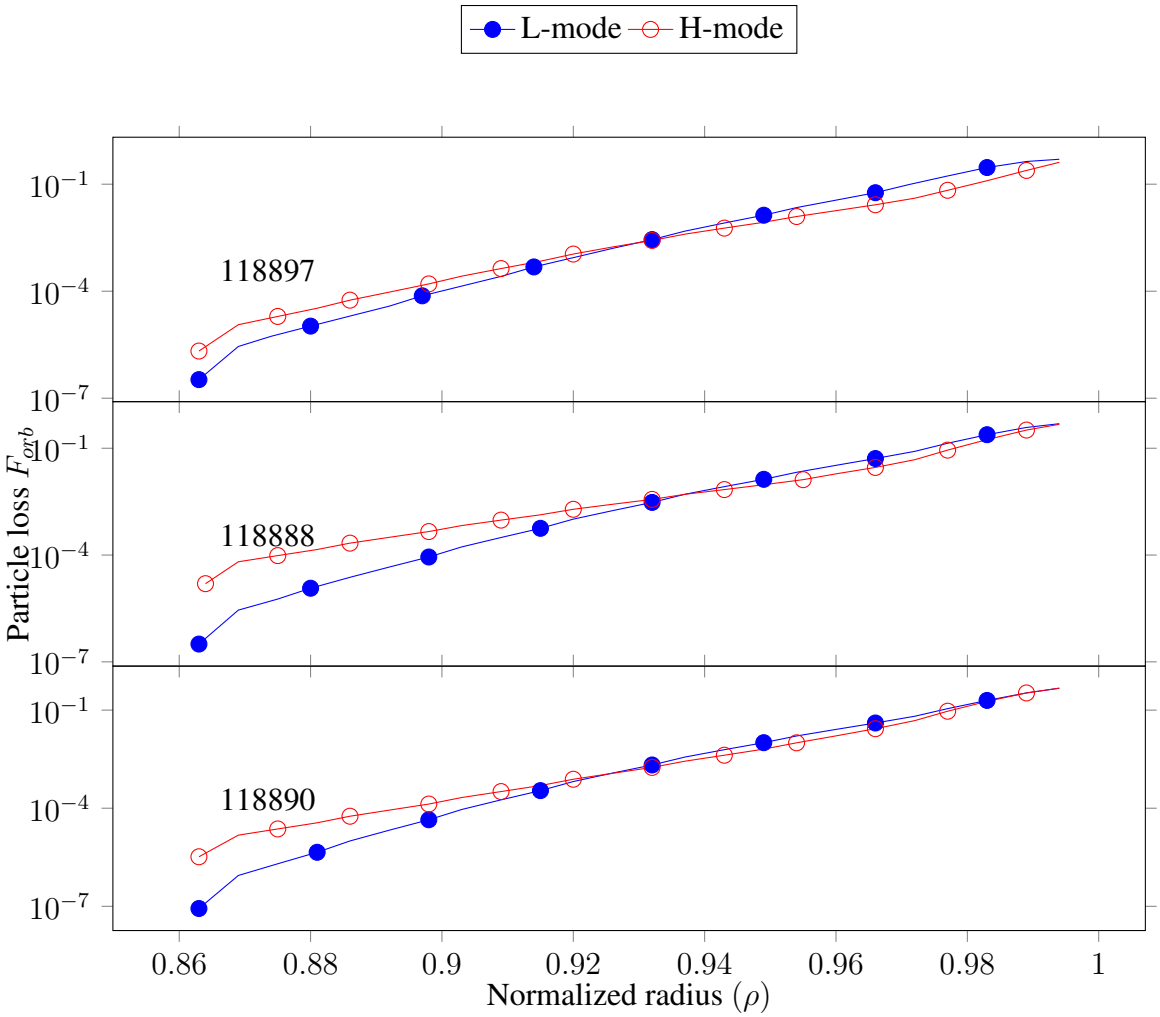

Figure 6.2: Ion orbit particle loss fractions F_{orb} for deuterium ($R_{loss} = 0.5$)

equal at $\rho = 0.994$ due to the comparably small increases in E_{min} and ion temperature.

6.2 Intrinsic Rotation

The preferential ion orbit loss of counter-current ions relative to co-current ions produces a net rotation of the remaining ions in the co-current ($\zeta_0 < 0$) direction. This intrinsic co-current rotation V_ϕ^{intrin} arises from the ion orbit momentum loss and contributes to the total experimental rotation, such that $V_\phi^{exp} = V_\phi^{intrin} + V_\phi^{fluid}$, where V_ϕ^{fluid} is the rotation due to the momentum in the plasma fluid. This effect is most influential in the edge where ion orbit loss is relatively large. The net co-current rotation velocity at a flux surface is

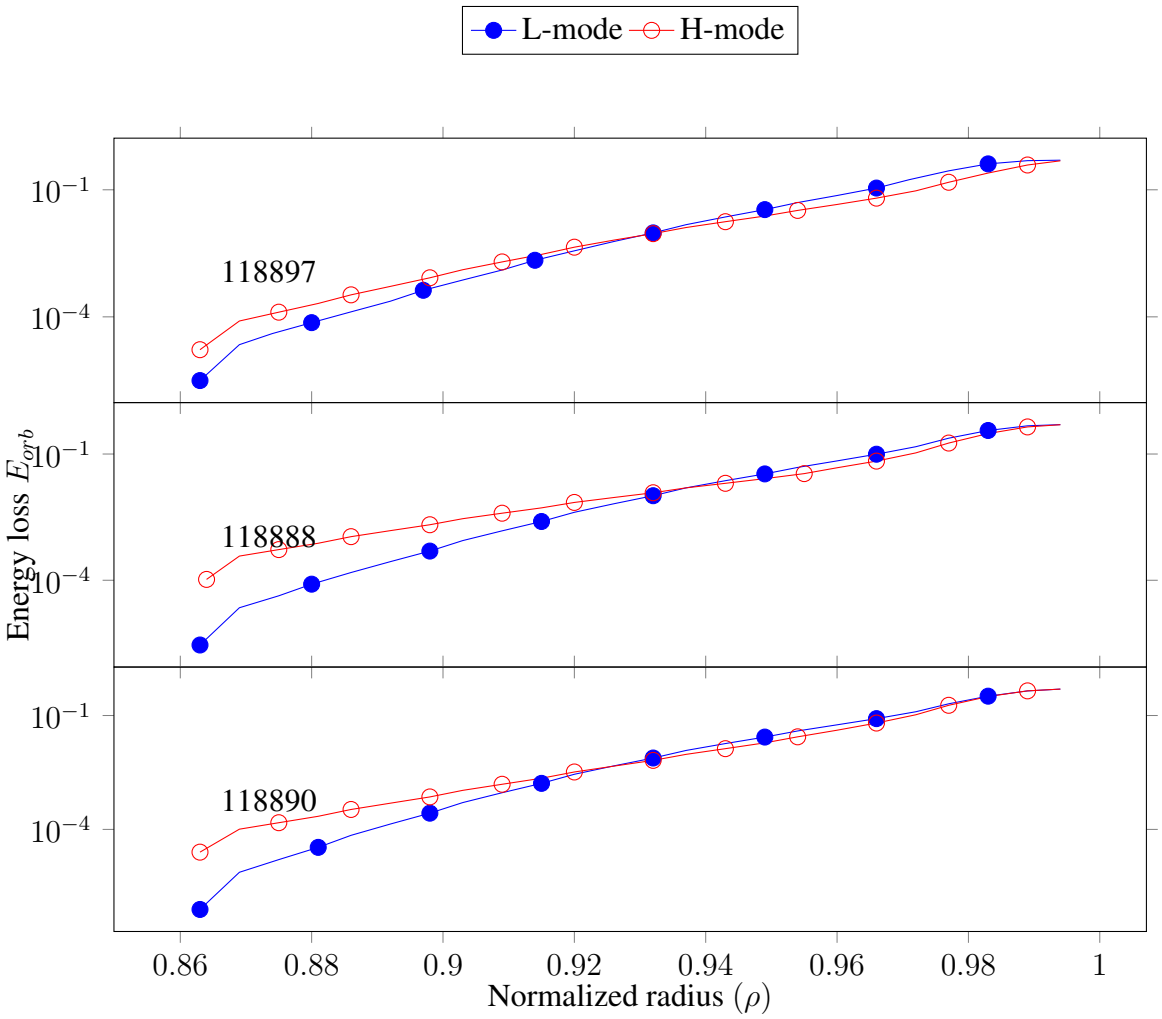

Figure 6.3: Ion energy loss fractions for deuterium E_{orb} ($R_{loss} = 0.5$)

determined using the cumulative net counter-current momentum loss fraction at that flux surface. An expression for the intrinsic toroidal rotation in terms of net momentum loss via IOL, M_{orb}, is

$$\begin{aligned} V_{\phi,k}^{intrin} &= \Delta V_{\phi,k} \\ &= 2\pi \int_{-1}^{1} d\zeta_0 \left[\int_{V_{min}(\zeta_0)}^{\infty} (V_0\zeta_0) V_0^2 f(V_0) dV_0 \right]_\rho \\ &= 4\pi M_{orb}(\rho) \left[\int_{0}^{\infty} (V_0) V_0^2 f(V_0) dV_0 \right]_\rho \\ &= 2\frac{\Gamma(2)}{\pi^{1/2}} M_{orb}(\rho) V_{th}(\rho) \\ &= \frac{2}{\pi^{1/2}} M_{orb}(\rho) \sqrt{\frac{2kT_{ion}(\rho)}{m}} \end{aligned} \tag{6.9}$$

The intrinsic rotation is plotted for carbon and deuterium ions in Fig. 6.4. It exhibits a peaking at about $\rho \approx 0.97$ for deuterium ions and $\rho \approx 0.98$ for carbon ions. The IOL of primarily ctr-current ions increases with radius out to a point just inside the LCFS at which most of the ctr-current ions have been lost and the co-current ions begin to be lost, resulting in a peaking of the co-current intrinsic rotation. IOL is greater in L-mode than in H-mode, resulting in a reduction of measured co-current rotation in H-mode relative to L-mode just inside the separatrix. This effect is apparent in discharge #118897, less so in #118888, and almost non-existant in #118890. This corresponds to the decrease in measured toroidal rotation in Fig. 5.4 being easily observable in #118897, barely discernible in #118888, and absent in #118890.

6.3 Radial Particle Flux

The flux surface averaged (FSA) ion particle continuity equation[10] in cylindrical geometry for the ion radial particle flux, $\Gamma_j(r) = n_j V_{r,j}$, is

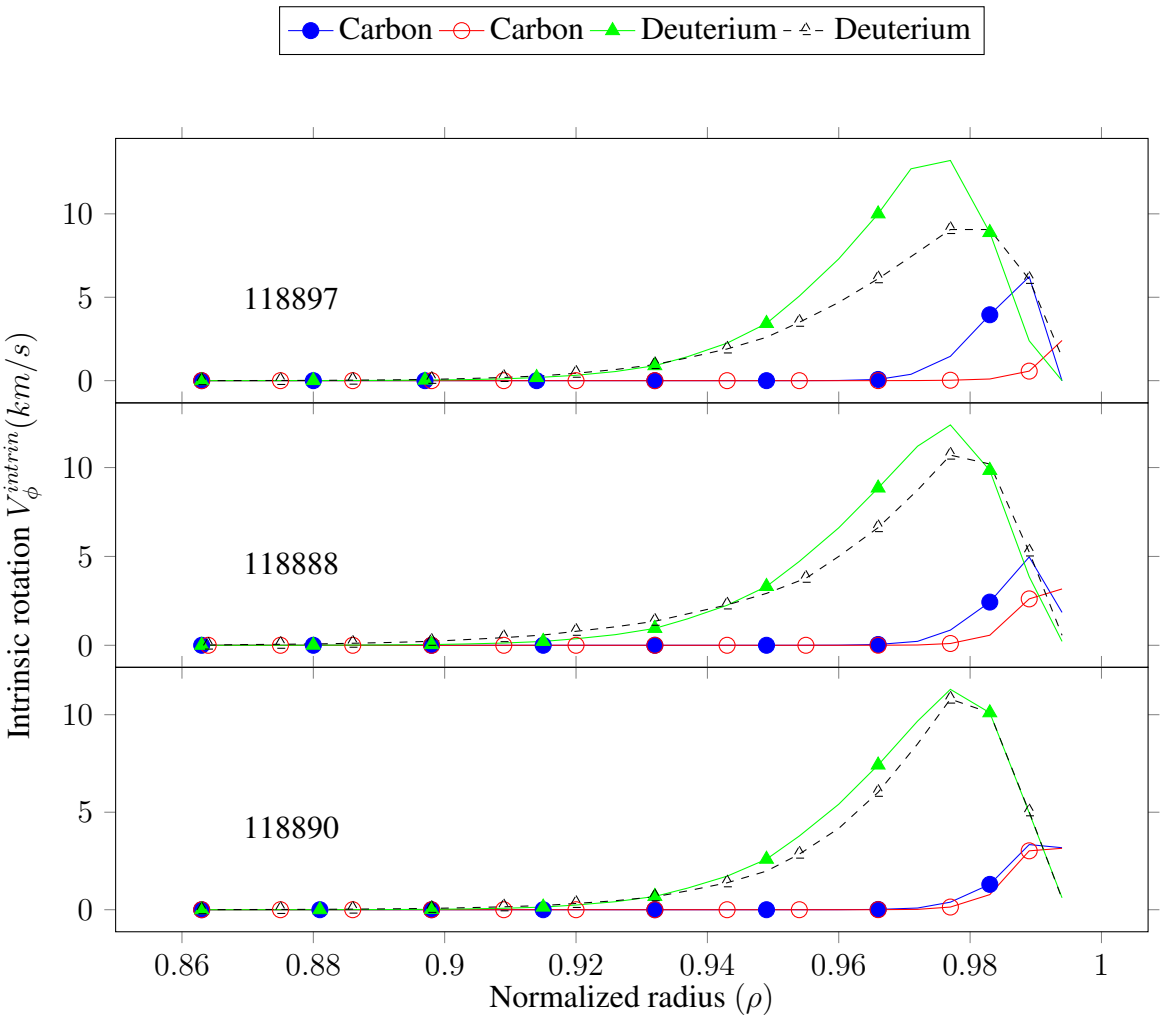

Figure 6.4: Deuterium and carbon intrinsic co-current toroidal rotation due to ion orbit loss (solid symbols L-mode, same empty symbols H-mode)

$$\frac{1}{r}\frac{\partial(rn_jV_{r,j})}{\partial r} \equiv \frac{1}{r}\frac{\partial(r\Gamma_j)}{\partial r} = -\frac{\partial n_j}{\partial t} + n_e n_o \langle\sigma\nu\rangle_{ion} + S_{nb,j}(1-\alpha f_{nb,j}^{iol}) - \alpha\frac{\partial F_{orb,j}}{\partial r}(\Gamma_j) \tag{6.10}$$

where the plasma is in an assumed steady state $\frac{\partial n_j}{\partial t} = 0$, and $n_e n_o \langle\sigma\nu\rangle_{ion}$ is the ionization of recycling neutrals calculated in GTEDGE. $S_{nb,j}$ is the fast ion source rate from neutral beams, which is calculated by the NBeams[28] code, $f_{nb,j}^{iol}$ is the differential IOL fraction for beam ions, and $\alpha = 2$ if charge neutrality of lost ions is maintained through an inward return current of thermalized plasma ions defined by Eq. (6.6) from the scrape-off layer. F_{orb} is the cumulative ion orbit loss for thermalized plasma ions. Subscript "j" refers to the main ion species. Using the integrating factor method, the radial particle flux is written.

$$\Gamma(r) = \frac{r_0}{r}\Gamma(r_0)e^{-2[F_{orb}(r)-F_{orb}(r_0)]} + \frac{1}{r}\int_{r_0}^{r} e^{-2[F_{orb}(r)-F_{orb}(r')]}S_n(r')r'dr' \tag{6.11}$$

where $S_n = n_e n_o \langle\sigma\nu\rangle_{ion} + S_{nb,j}(1-\alpha f_{nb,j}^{iol})$ is the total source rate, r is an arbitrary flux surface radius, and r_0 is an innermost flux surface radius such that $r_0 < r$. The first term is the particle flux at r_0 being attenuated as it propagates toward r. The second term is the summation of each source attenuated as they propagate outward to r. $\frac{r_0}{r}$ and $\frac{r'}{r}$ terms represent the outward flowing particles occupying a larger volume as they propagate outward. In GTEDGE, the radii are expressed as normalized radii, where $\rho_0 = 0$ and $\rho \approx 0.864$ in the core calculation, and $\rho_0 = 0.864$ and $\rho = 1$ in the edge calculation.

To get the particle flux at r_0, the source rate must be calculated from the NBeams[28] deposition profile. We begin by balancing the total power injected into the core.

$$NB_{dep,n}(\rho) = \left(\frac{0.624 * 10^{22}P_{beam}[MJ]}{E_{nbi}[KeV]/n}\right)\left(\frac{fb_n H(\rho)}{V_P}\right)[1 - ffrac(\rho)] \tag{6.12}$$

where P_{beam} is the neutral beam power injected into the plasma, E_{nbi} is the average energy of the neutral beams, $ffrac(\rho)$ is the differential fraction of fast ions that have become ion orbit lost before thermalizing, $H(\rho)$ is the deposition profile from NBeams, V_P is the plasma volume, and fb_n is the fraction of NBI power imparted to neutrals that are injected as deuterium molecules containing n deuterium atoms. Depending on the energy of the neutral beam injection system, some neutrals will be one deuterium atom of energy E_{nbi}, two atoms of energy $E_{nbi}/2$ per deuterium, or three atoms of energy $E_{nbi}/3$ per deuterium. This needs to be calculated for n = 1, 2, and 3 and summed together to obtain a total deposition profile. If we assume that the plasma is in a quasi-steady-state condition, then this will provide the total source rate into the core, and therefore the total sink rate out of the core, as neutrals do not penetrate far enough into the plasma.

Then the source rates must be multiplied by their respective volumes, summed together, and divided by the plasma area at ρ_0.

$$\Gamma(r_0) = \frac{\int_0^{r_0} NB_{dep}(\rho)V(\rho)d\rho}{A(\rho_0)} \tag{6.13}$$

Now we have our boundary condition for the edge plasma radial particle flux at r_0. This method is performed throughout the entire plasma, meaning that the neutral beam source is also calculated for the edge.

Figure 6.5 shows the radial particle flux for deuterium from Eq. (6.11). All the discharges show similar behavior. The radial particle flux increases with ρ in the edge due to ionization of recycling neutrals, but then peaks at $\rho \simeq 0.98$ and decreases due to thermalized ion orbit losses becoming larger than ionization in the edge region. After the L-H transition, the ionization of neutrals increases strongly in the edge, and ion orbit loss decreases, resulting in an increase in the outward ion particle flux. In H-mode, the steep radial gradient in both IOL and ionizing neutrals near the separatrix results in a steeper gradient in the radial particle flux near the separatrix in H-mode relative to L-mode. For shot #118890, the radial particle flux does not change strongly between L-mode and H-mode, likely due

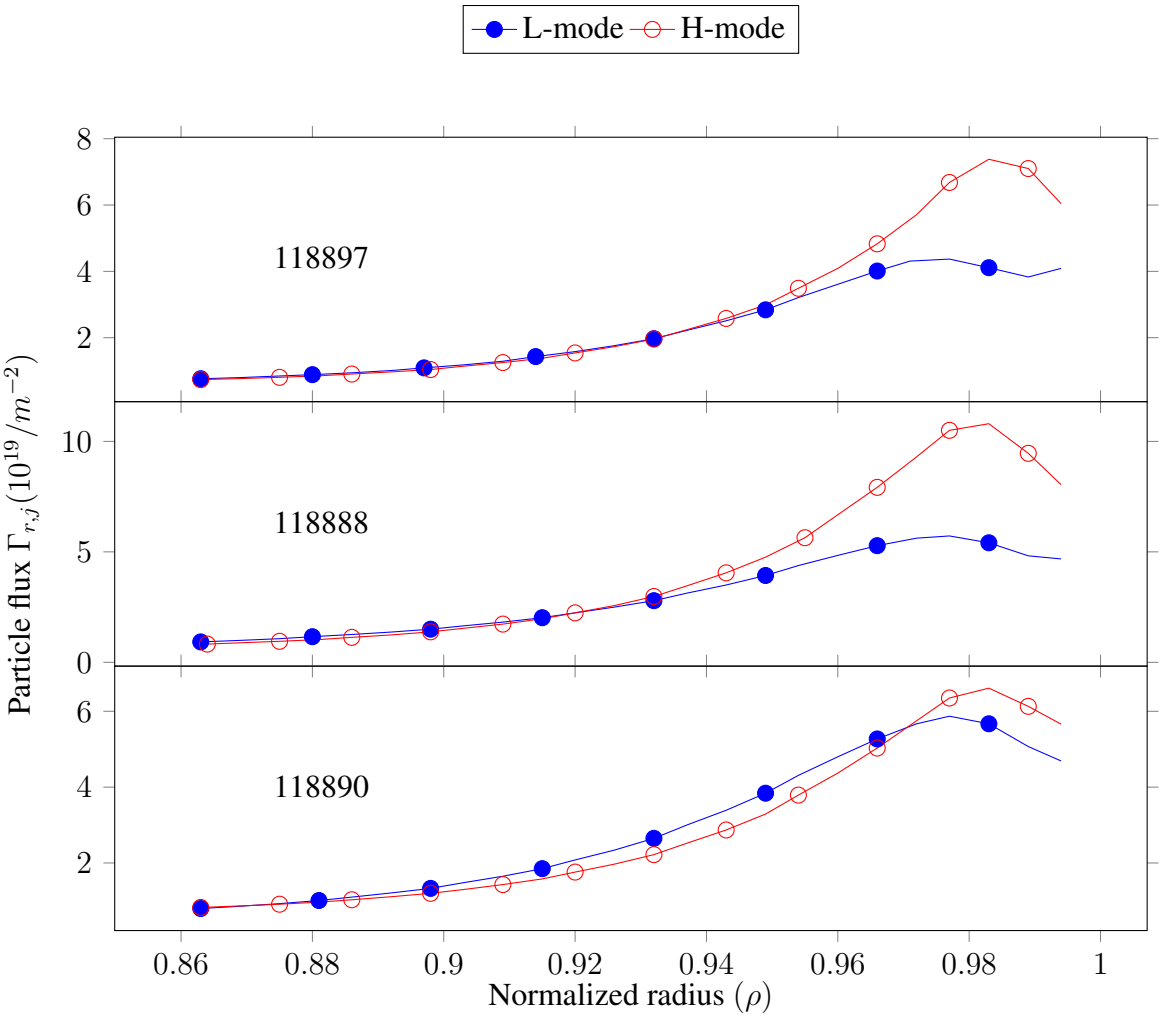

Figure 6.5: Deuterium Radial Particle Flux

to their similar neutral densities and particle loss fractions.

CHAPTER 7
MOMENTUM TRANSPORT FREQUENCY AND THE PINCH DIFFUSION EQUATION

7.1 Pinch Velocity

The toroidal component of the momentum balance equation for main ions can be written[29]

$$n_j m_j[(\nu_{j,k}+\nu_{d,j})V_{\phi,j}-\nu_{j,k}V_{\phi,k}] = n_j e_j E_\phi^A + n_j e_j B_\theta V_{r,j} + M_{\phi,j} \tag{7.1}$$

where j and k refer to deuterium and carbon respectively, and there is a similar equation with the subscripts "j" and "k" interchanged for the impurity ions. E_ϕ^A is the induced toroidal electromagnetic field, M_ϕ is momentum input via external sources such as neutral beams, B_θ is the poloidal magnetic field, and $\nu_{j,k}$ is the collisional momentum transfer frequency between species j and k. $\nu_{d,j}$ is the total toroidal angular momentum transfer frequency. It represents the combined effects of processes such as viscosity, inertia, atomic physics and anomalous processes.[30] $\nu_{d,j} = \nu_{visc}+\nu_{in}+\nu_{atom}$. The flux surface averaged neo-classical viscous toroidal torque is written $\langle R^2\nabla\phi\cdot\nabla\cdot\prod\rangle \simeq Rnm\nu_{visc}V_\phi$, the inertial torque is written $\langle R^2\nabla\phi\cdot\nabla nm(\overrightarrow{V}\cdot)\overrightarrow{V}\rangle \simeq Rnm\nu_{in}V_\phi$, $\nu_{atom} = \nu_{cx}+\nu_{ion}$, and ν_{visc} is a viscous momentum exchange frequency, including neoclassical and turbulent processes. ν_{cx} and ν_{ion} are momentum transfer frequencies from charge exchange and ionization respectively.

Assuming that there is only one impurity ion species "k" with the same logarithmic derivative and local temperature as species "j", the radial momentum balance for species "j"[22]

$$V_{\phi,j} = \frac{1}{B_\theta}\left[E_r + V_{\theta,j}B_\phi - \frac{1}{n_j e_j}\frac{\partial p_j}{\partial r}\right] \tag{7.2}$$

can be combined with the toroidal momentum balance Eq. (7.1) to obtain a constraint on the main ion pressure gradient.

$$-\frac{1}{p_j}\frac{\partial p_j}{\partial r} = \frac{V_{r,j} - V_{r,j}^{pinch}}{D_j} \tag{7.3}$$

where the diffusion coefficient D_j is defined

$$D_j \equiv \frac{m_j T_j \nu_{j,k}}{(e_j B_\theta)^2}\left(1 + \frac{\nu_{d,j}}{\nu_{j,k}} - \frac{e_j}{e_k}\right) \tag{7.4}$$

and the "pinch velocity" defined as

$$V_{r,j}^{pinch} \equiv \frac{[-M_{\phi,j} - n_j e_j E_\phi^A + n_j m_j(\nu_{j,k} + \nu_{d,j})(f_p^{-1} V_{\theta,j} + E_r/B_\theta) - n_j m_j \nu_{j,k} V_{\phi,k}]}{n_j e_j B_\theta} \tag{7.5}$$

is the collection of normalized, mainly electromagnetic forces affecting particle transport, where $f_p = \frac{B_\theta}{B_\phi}$. The constraint of Eq. (7.3) on the main ion pressure gradient can be rearranged into a form that clearly shows the diffusive and non-diffusive components of the radial particle flux[30].

$$\begin{aligned}\Gamma_j \equiv n_j V_{r,j} &= -\frac{n_j D_j}{p_j}\frac{\partial p_j}{\partial r} + n_j V_{r,j}^{pinch} \\ &= -D_j \frac{\partial n_j}{\partial r} - D_j \frac{n_j}{T_j}\frac{\partial T_j}{\partial r} + n_j V_{r,j}^{pinch}\end{aligned} \tag{7.6}$$

The momentum transport frequencies $\nu_{d,j}$ and $\nu_{j,k}$ are significant to the calculation of the diffusion coefficient and the pinch velocity. If both the carbon and deuterium rotation velocities are measured, $\nu_{d,j}$ can be inferred by using the measured toroidal rotation data and the calculated radial particle flux to solve Eq. (7.1) and the equivalent equation with "j" and "k" interchanged for $\nu_{d,j}$ and $\nu_{d,k}$. Since the deuterium rotation velocities are

not measured for this discharge, as is now becoming possible,[31] the momentum transfer frequency $\nu_{d,j}$ must be calculated from perturbation theory[29], as discussed below.

The toroidal momentum balance Eq. (7.1) for both species can be added together to eliminate the friction terms, and define an "effective" drag frequency[29].

$$\begin{aligned}\nu_d^{eff} &\equiv \frac{n_j m_j \nu_{d,j} + n_k m_k \nu_{d,k}}{n_j m_j + n_k m_k} \\ &= \frac{(n_j e_j E_\phi^A + e_j B_\theta \Gamma_{r,j} + M_{\phi,j}) + (n_k e_k E_\phi^A + e_k B_\theta \Gamma_{r,k} + M_{\phi,k}) - \{n_j m_j \nu_{d,j}(V_{\phi,j} - V_{\phi,k})\}}{(n_j m_j + n_k m_k) V_{\phi,k}}\end{aligned} \tag{7.7}$$

Since $n_j \gg n_k$ & $\Gamma_{r,j} \gg \Gamma_{r,k}$, and the deuterium radial particle flux is the dominant term in Eq. (7.7), it can be approximated that $\nu_{d,j} \approx \nu_d^{eff}$. In previous work[29] the difference in toroidal velocities was set to zero ($V_{\phi,j} - V_{\phi,k} = \Delta V_\phi = 0$) to obtain a zeroth-order approximation of this effective momentum transport frequency. This was then used to obtain a first-order approximation of ΔV_ϕ and $\nu_{d,k}$.

In this paper, which takes into account intrinsic rotation, the zeroth order difference in toroidal velocities of the two species is set equal to the difference between their respective intrinsic rotations, $(V_{\phi,j} - V_{\phi,k})_0 = (\Delta V_\phi)_0 \approx V_{\phi,j}^{intrin} - V_{\phi,k}^{intrin} = \Delta V_\phi^{intrin}$ to obtain an approximation of the deuterium momentum transfer frequency, as well as the deuterium toroidal rotation. Setting $\nu_{d,j} = \nu_d^{eff}$ and solving for $\nu_{d,j}$ results in

$$\nu_{d,j}^1 \approx \nu_{d,j} = \frac{n_j e_j E_\phi^A + e_j B_\theta \Gamma_{r,j} + M_{\phi,j} + n_k e_k E_\phi^A + e_k B_\theta \Gamma_{r,k} + M_{\phi,k}}{(n_j m_j + n_k m_k) V_{\phi,k} + n_j m_j \Delta V_\phi^{intrin}} \tag{7.8}$$

The inferred drag frequency, $\nu_{d,j}$ including IOL, is plotted for discharges #118897, #118888 and #118890 in Fig. 7.1. The drag frequency of discharge #118897 becomes greater in H-mode for $\rho > 0.95$ and exhibits a peaking structure. Discharge #118888

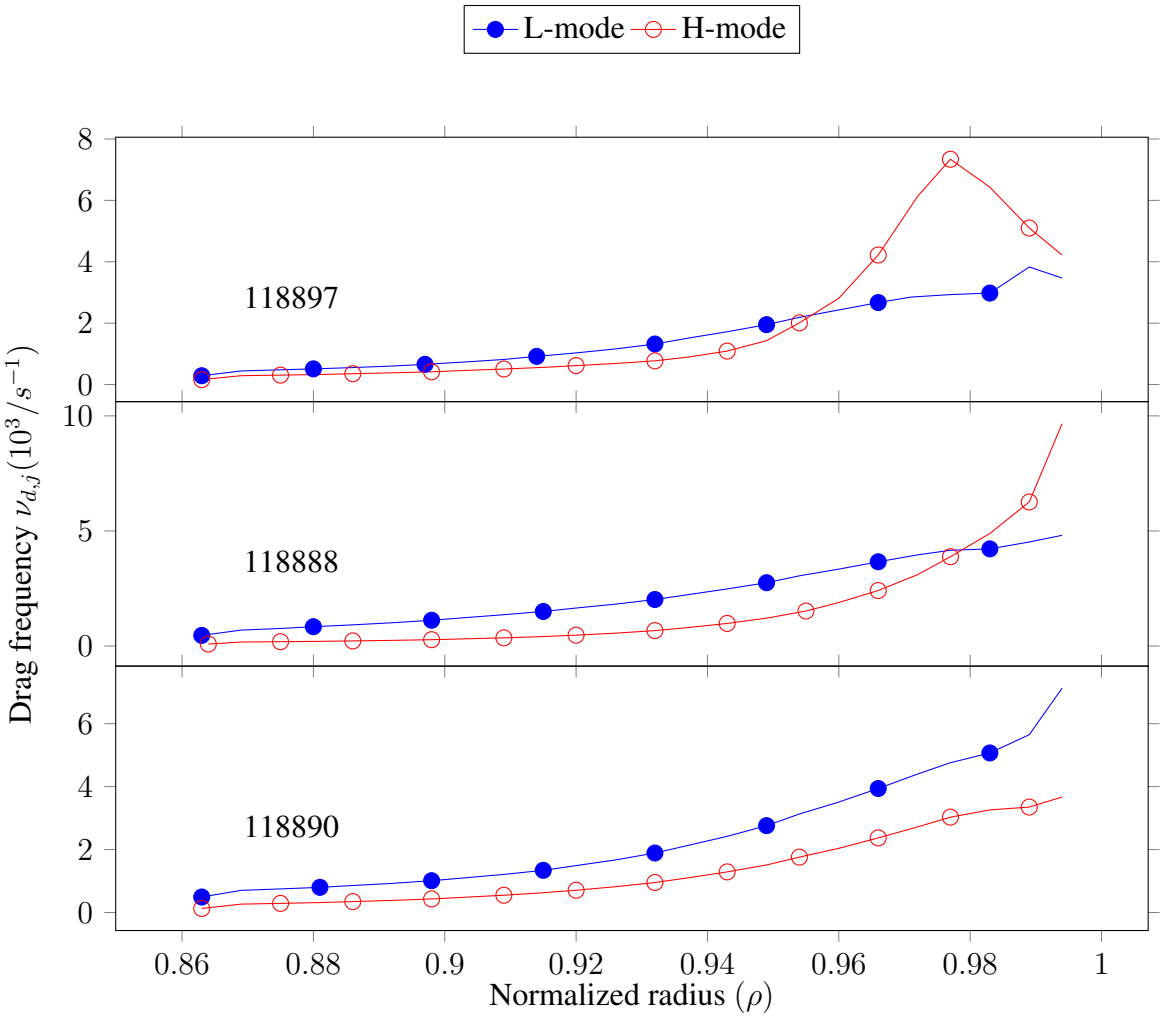

Figure 7.1: Deuterium Drag Frequencies

also shows an increased drag frequency in the edge after the L-H transition, but does not exhibit a peaking behavior. This increase in drag frequency for $\rho > 0.98$ after the L-H transition is consistent with the decrease in IOL and intrinsic rotation, and agrees with previous work[12], However, the drag frequency for discharge #118890 decreases slightly after the L-H transition throughout the edge region. This is likely because there is little to no change in IOL or intrinsic rotation in shot #118890 after the L-H transition. This aspect of the results requires further investigation.

The pinch velocity of Eq. (7.5) is also strongly dependent on the deuterium poloidal velocity. This is calculated from the radial momentum balance for deuterium[12] using the

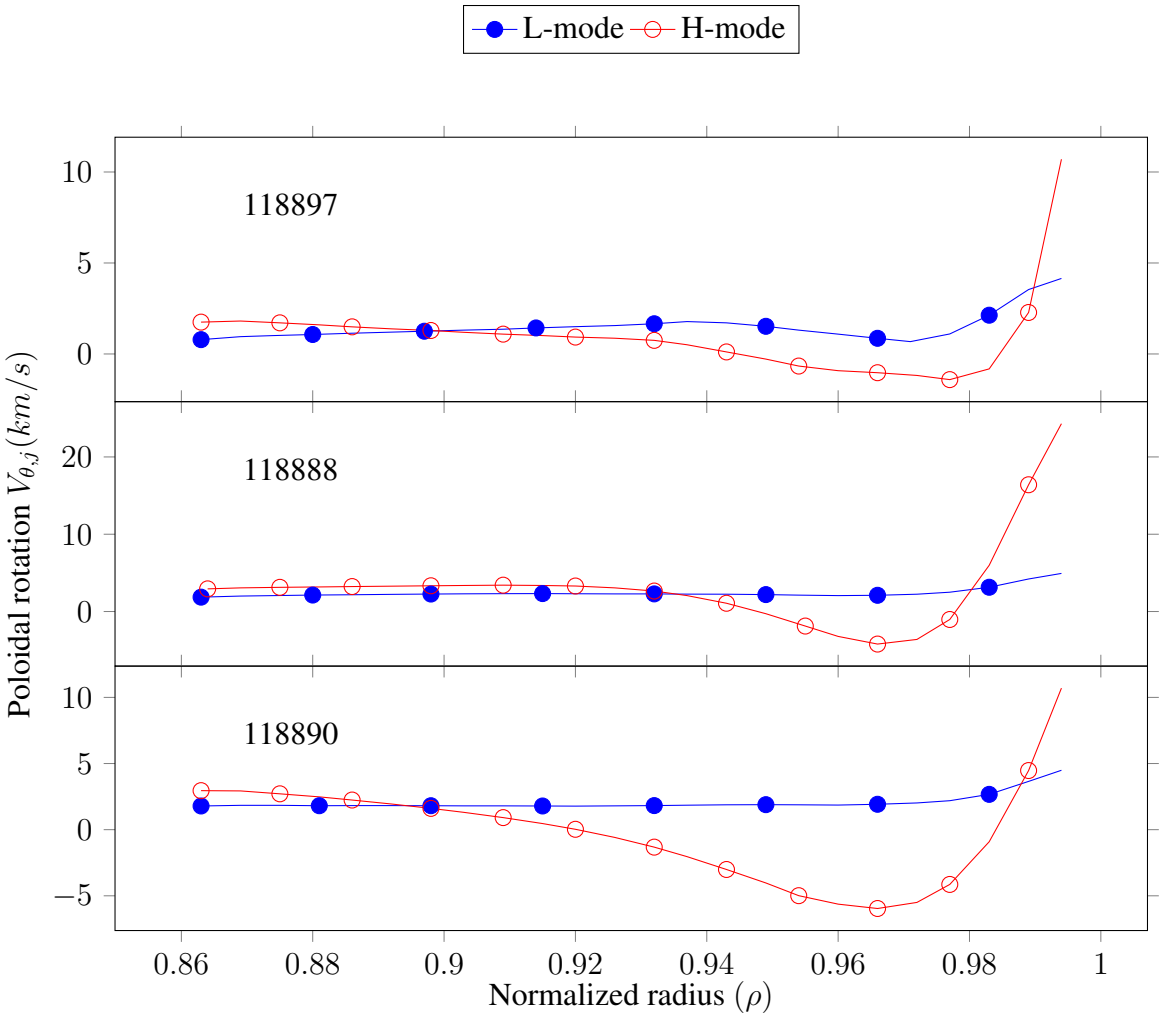

Figure 7.2: deuterium poloidal rotation profiles

perturbation estimate for the deuterium toroidal velocity.

$$V_{\theta,j} = \left[-E_r^{exp} + V_{\phi,j} B_\theta + \frac{1}{n_j e_j} \frac{\partial p_j}{\partial r} \right] \frac{1}{B_\phi} \tag{7.9}$$

Figure 7.2 shows the deuterium poloidal velocity for the three discharges. For all discharges the deuterium poloidal velocity is similar in structure to the radial electric field profile (Fig. 5.6). It remains relatively flat in L-mode. After the L-H transition, the poloidal velocity becomes negative for $\rho > 0.92$, obtains a maximum negative value at $\rho \approx 0.965$, then increases above its L-mode value near the separatrix.

The pinch velocity of Eq. (7.5), which is a primarily electromagnetic component of the

radial particle flux (i.e. a primarily electromagnetic normalized radial force), is shown in Fig. 7.3. The main result of Fig. 7.3 is that the electromagnetic pinch velocity increases from weakly inward in L-mode to strongly inward in H-mode for all three discharges. Immediately after the L-H transition, a strong inward pinch develops for $\rho > 0.95$ for all 3 discharges. The decrease in intrinsic rotation for $\rho > 0.94$ in H-mode causes an increase in the momentum transfer frequency, which, in conjunction with the increase in the deuterium poloidal velocity, increases the magnitude of the pinch velocity. Despite all 3 discharges having comparable radial electric field magnitudes, the pinch velocity of #118888 in H-mode for $\rho > 0.98$ is 3 times larger in magnitude than it is for discharges #118897 and #118890. This is likely due to the much larger calculated deuterium poloidal velocity in H-mode for discharge #118888 (Fig. 7.2).

Figures 7.4 and 7.5 are plots of the main components contributing to the pinch velocity. These plots show that the pinch velocity is primarily dependent on the V_θ term, the third term of Eq. (7.5), whereas the E_r term is responsible for structure in the $V_{r,j}^{pinch}$ profiles. The pinch velocity and its components have similar structure in the L-mode for all 3 discharges, being slightly negative (inward) in the edge. After the L-H transition, the pinch velocity of all 3 discharges increases in magnitude, and the radial derivative also increases strongly with radius. Discharge #118888 is the greatest in magnitude because the deuterium poloidal velocity is over 5 times greater in H-mode than the other 2 discharges.

7.2 Comparison with Previous Work

As discussed in the previous section, Eq. (7.7) was previously approximated by setting the difference in toroidal velocities of the two ion species to zero ($V_{\phi,j} - V_{\phi,k} = \Delta V_\phi = 0$). In this paper, the zeroth order difference in toroidal velocities of the two species is set equal to the difference between their respective intrinsic rotations, $(V_{\phi,j} - V_{\phi,k})_0 = (\Delta V_\phi)_0 \approx V_{\phi,j}^{intrin} - V_{\phi,k}^{intrin} = \Delta V_\phi^{intrin}$. The two perturbation methods have been compared with data from a DIII-D discharge (#149468) in which the deuterium toroidal velocity was measured.

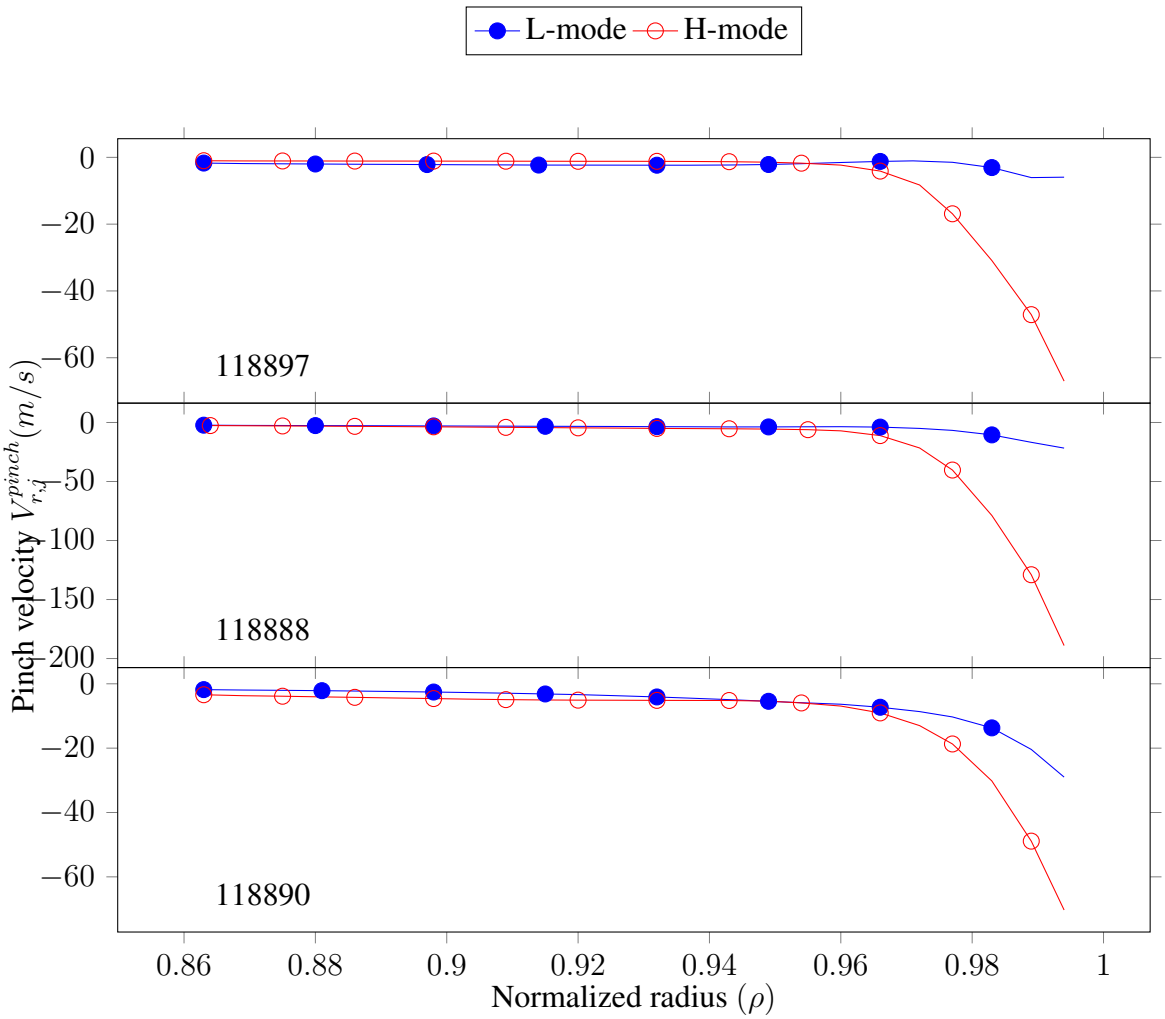

Figure 7.3: Pinch Velocity (+ out, - in)

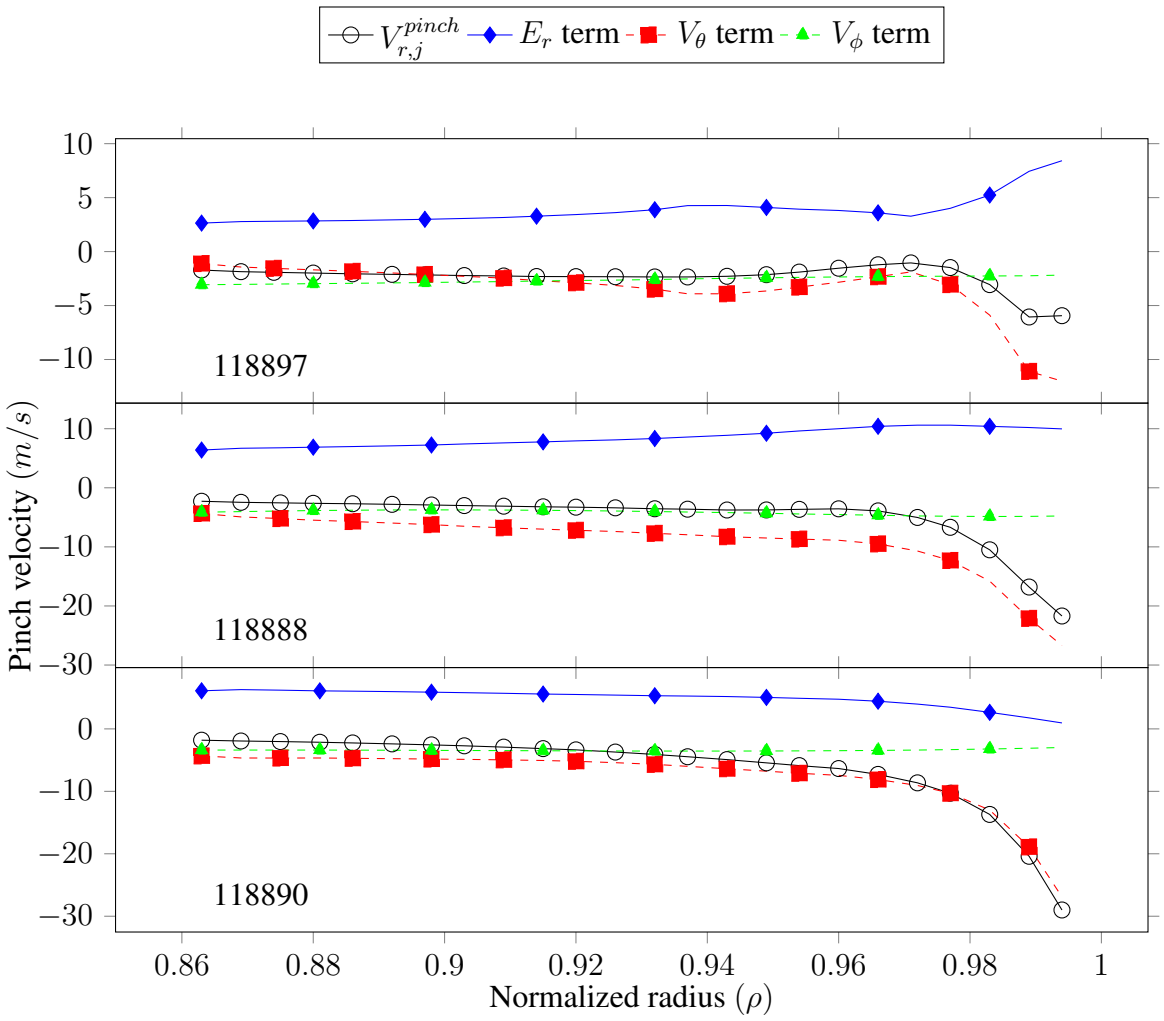

Figure 7.4: Pinch Velocity Components (L-mode)

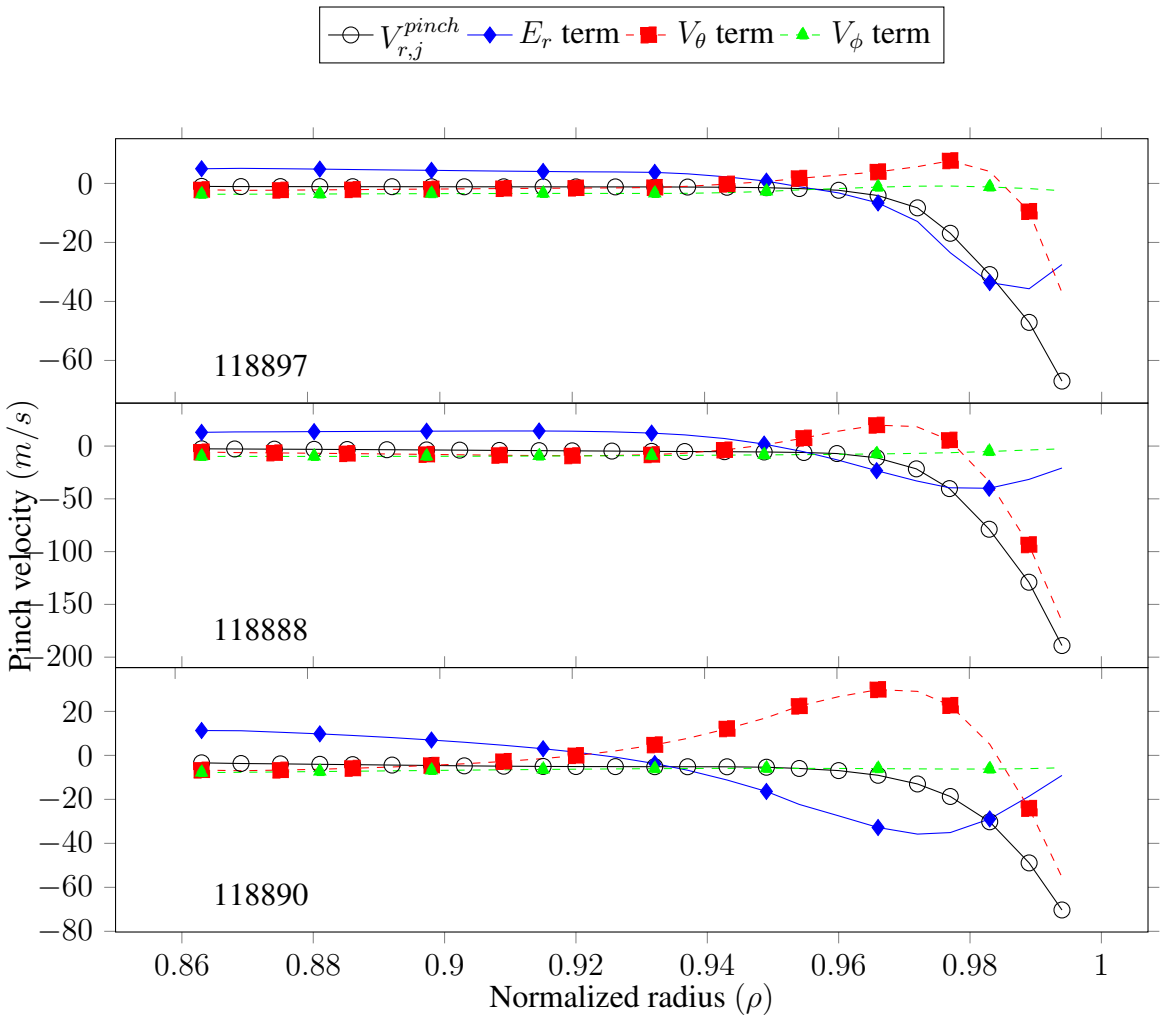

Figure 7.5: Pinch Velocity Components (H-mode)

The CER measured values of both the carbon (solid squares) and deuterium (empty circles) are plotted in Fig. 7.6, along with the original perturbation theory estimate, $V_{\phi,j}^{pert}$ neglecting IOL (solid circles) and the improved perturbation estimate taking IOL into account (solid triangles). Clearly, taking IOL into account improves the perturbation estimate for $0.86 < \rho < 0.97$. We note that the measured and calculated $V_{\phi,j}$ diverge as they near the separatrix, and the reason for this is not yet understood.

Figure 8 of Ref. [32] shows a similar comparison of measured and perturbation estimates of deuterium toroidal velocity. In the previous work, the perturbation estimate deviates from the measured rotation, and the deviation increases with radius, as also shown in Fig. 7.6 here. By including ion orbit loss in the estimate of ΔV_ϕ, we are able to more accurately calculate the experimental deuterium velocity up to about $\rho \approx 0.955$, at which point it begins to deviate from the measured value. The deviation remains more accurate with IOL included rather than without, until approximately $\rho \approx 0.975$, at which point the perturbation method results intersect, and inclusion of IOL no longer increases the accuracy of the $V_{\phi,j}$ calculation. In fact, the accuracy is slightly decreased near the separatrix.

Discharge #149468 occurred in 2012, the year in which the deuterium diagnostic system was implemented. There were very few edge chords during this experiment, and many have been added since then. Also, the data analysis tools used for this discharge have improved since. Therefore, there is a significant lack of spatial resolution and reliability close to the separatrix. However, Ref. [33] shows that the improved CER measurements of deuterium toroidal velocity agree with previous measurements. Therefore, while this perturbation theory is an improvement for $\rho < 0.95$, the inclusion of intrinsic rotation is not sufficient to calculate the difference between the carbon and deuterium velocities near the separatrix.

Since the calculation of the pinch velocity from Eq. (7.5) largely depends on the drag frequency Eq. (7.8), as well as the deuterium poloidal velocity Eq. (7.9), it is a concern that the calculation of the pinch velocity is also not sufficient for $\rho > 0.95$ due to its reliance on

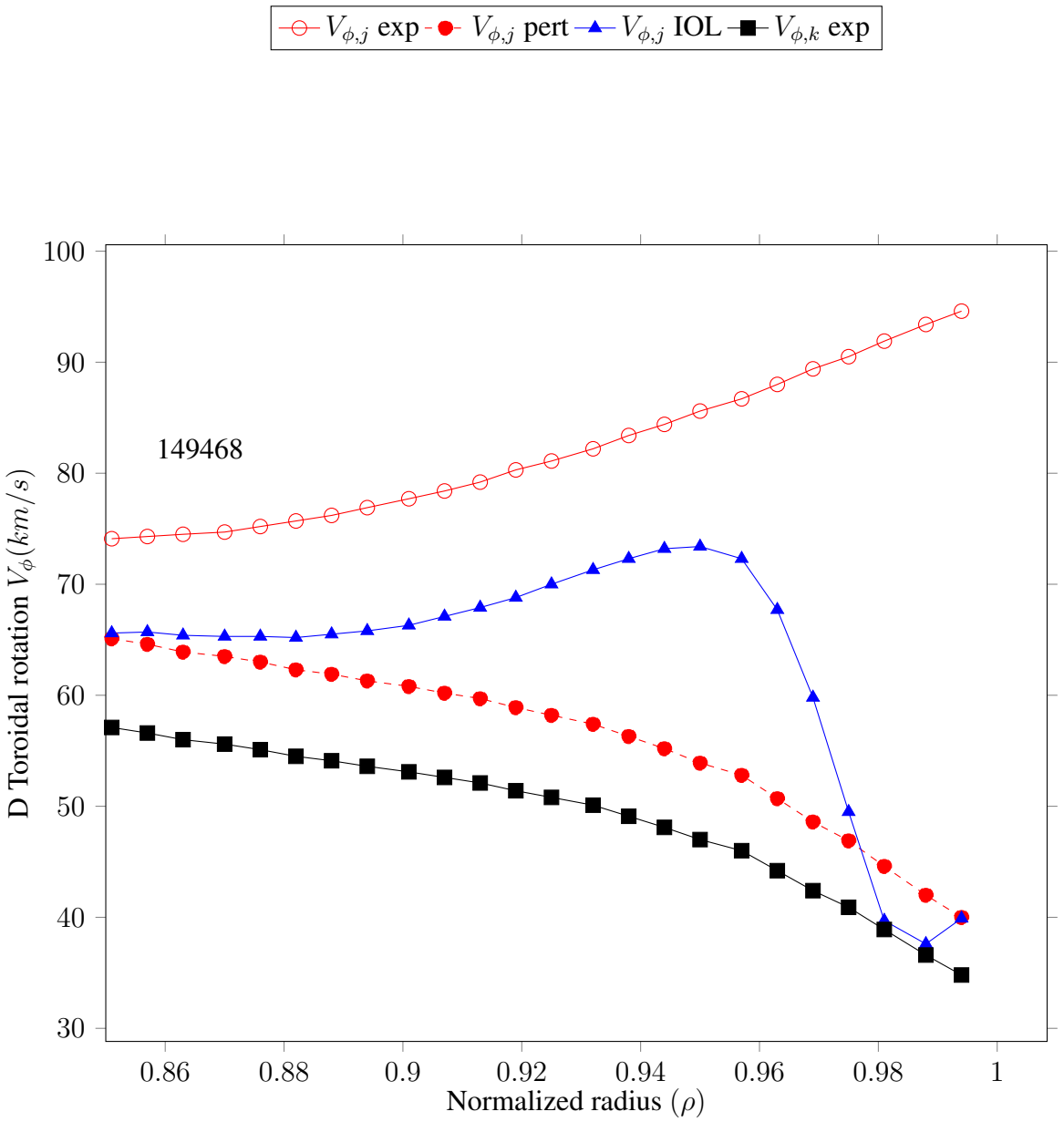

Figure 7.6: Comparison of measured and perturbation estimates of deuterium toroidal velocity in DIII-D shot #149468 (Measured $V_{\phi,D}$ is denoted by empty circles, the perturbation theory estimate not including IOL by solid circles, the perturbation theory estimate including IOL by solid triangles, and the measured $V_{\phi,C}$ by solid squares).

terms that are calculated from perturbation theory[29]. Figure 7.7 shows a comparison of the pinch velocity calculated using two different methods for DIII-D discharge #149468. The pinch velocity calculated using measured values of $V_{\phi,j}$ is denoted by empty circles, whereas the pinch velocity calculated using rotation velocities obtained via perturbation theory[29] is denoted by solid triangles.

Figure 7.7 shows that the pinch velocity calculated from deuterium rotation obtained via perturbation theory has an identical structure to that of the pinch velocity calculated from experimental rotation data. The "perturbation" $V_{r,j}^{pinch}$ is about $10m/s$ less than the "experimental" $V_{r,j}^{pinch}$ everywhere in the edge plasma. What is interesting about this finding is that for $\rho > 0.95$, although the perturbation estimate of the deuterium toroidal rotation deviates from the measured value, the pinch velocity does not deviate. This is due to the fact that the corresponding deviations in drag frequency $\nu_{d,j}$ and deuterium poloidal velocity $V_{\theta,j}$ have opposing effects on the pinch velocity. The drag frequency increases in magnitude, whereas the deuterium poloidal velocity decreases in magnitude. These terms are multiplied together in the calculation of $V_{r,j}^{pinch}$ in Eq. (7.5), mitigating one another's deviations from the value calculated from experimental data.

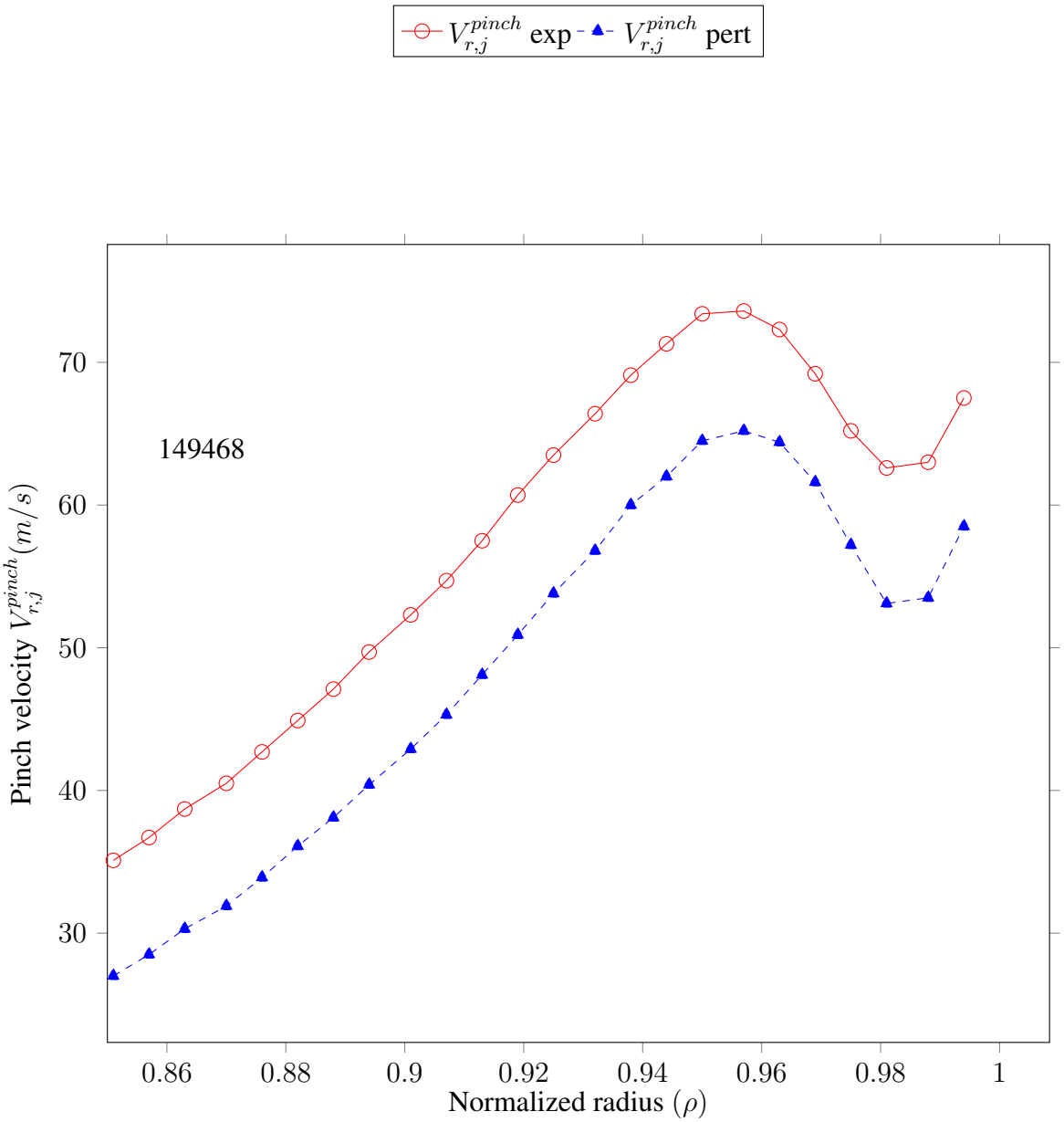

Figure 7.7: Comparison of Pinch Velocity (+ out, - in) calculations in DIII-D shot #149468 ($V_{r,j}^{pinch}$ from measured deuterium rotation is denoted by empty circles, and $V_{r,j}^{pinch}$ from velocities calculated using perturbation theory by solid triangles).

CHAPTER 8

CONCLUSIONS

Two interesting new L-H phenomena have been examined in a series of DIII-D discharges. 1) The measured carbon co-I toroidal rotation for $\rho < 0.94$ was observed to increase at the L-H transition, as expected, but the measured rotation velocity actually decreased for $\rho > 0.94$. A particle-momentum-energy balance analysis shows that the preferential ion orbit loss of ctr-I ions causes a co-I intrinsic rotation for $\rho > 0.94$ which is greater in L-mode than in H-mode, thus causing the drop in total measured rotation for $\rho > 0.94$ at the L-H transition. This is a short lived phenomena. Shortly afterward, the intrinsic rotation and the total measured rotation are expected to increase above their L-mode values. 2) In all of the three shots examined the electromagnetic pinch velocity required for momentum conservation went from weakly inward in L-mode to strongly inward in H-mode for $\rho > 0.96$, consistent with improved particle confinement in H-mode being associated with larger inward electromagnetic forces on the ions in H-mode compared to L-mode.

An ion orbit loss calculation was performed by combining canonical toroidal momentum balance with conservation of energy and magnetic moment to derive a quadratic equation that can be solved to determine particle, energy, and momentum loss fractions. A reduction in the particle and energy loss fractions for $\rho > 0.9$ after the L-H transition indicates decreased ion orbit loss in the far edge in the H-mode relative to L-mode.

Ctr-current ions are preferentially lost, resulting in a co-current net intrinsic rotation. The intrinsic rotation increases with radius until $\rho \approx 0.95$, at which point co-current ions are becoming lost, resulting in a peak in the intrinsic rotation. The peak in the intrinsic rotation is greater in L-mode than in H-mode, consistent with greater IOL in L-mode. The reduction in intrinsic rotation in H-mode causes the reduction in the measured carbon toroidal rotation for $\rho > 0.94$ immediately after the L-H transition.

Appendices

APPENDIX A

TEMPORAL DATA FOR SELECTED DISCHARGES

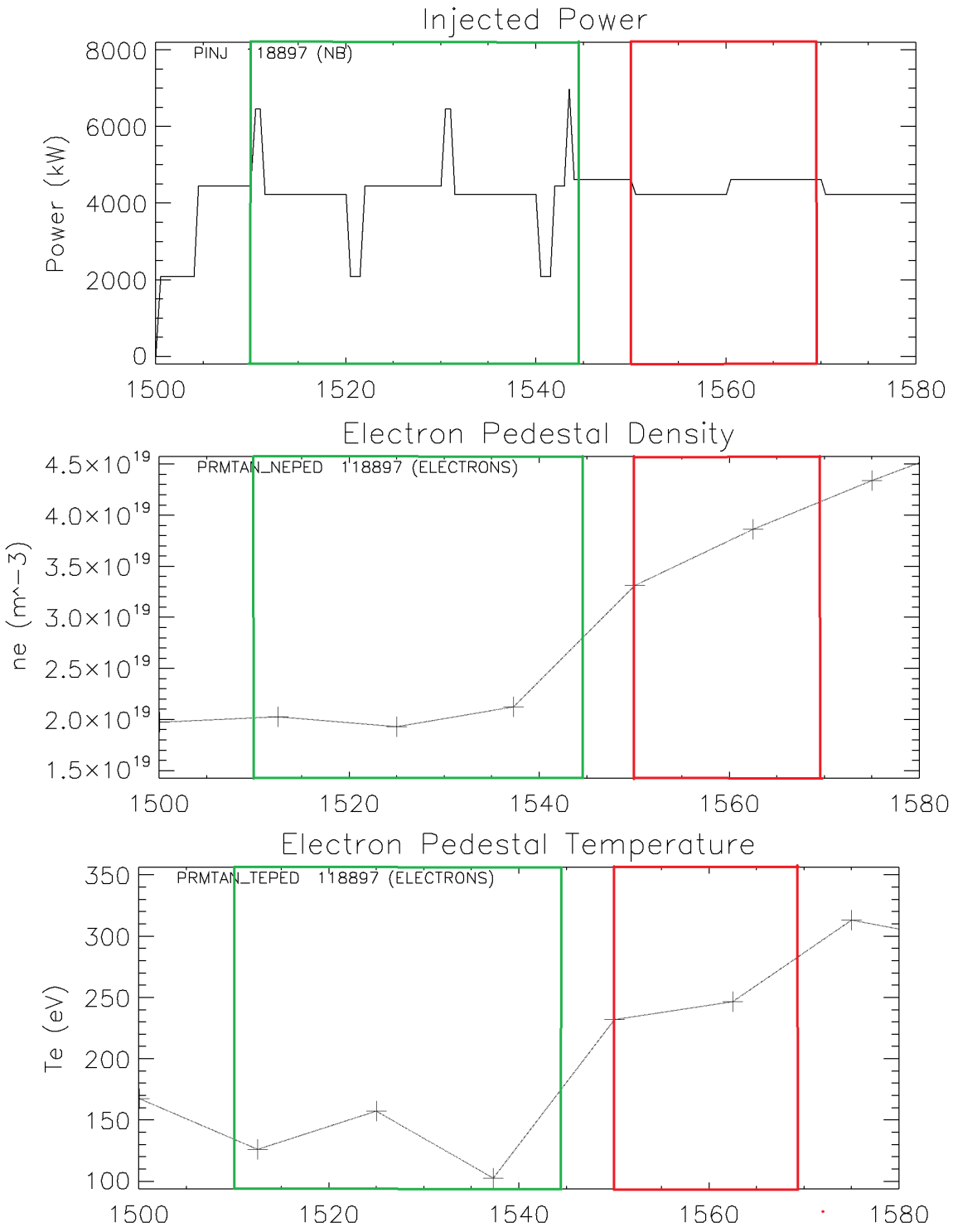

Figure A.1: Time dependent experimental data for shot #118897. The leftmost box is the L-mode time-slice, and the rightmost box is the H-mode time-slice

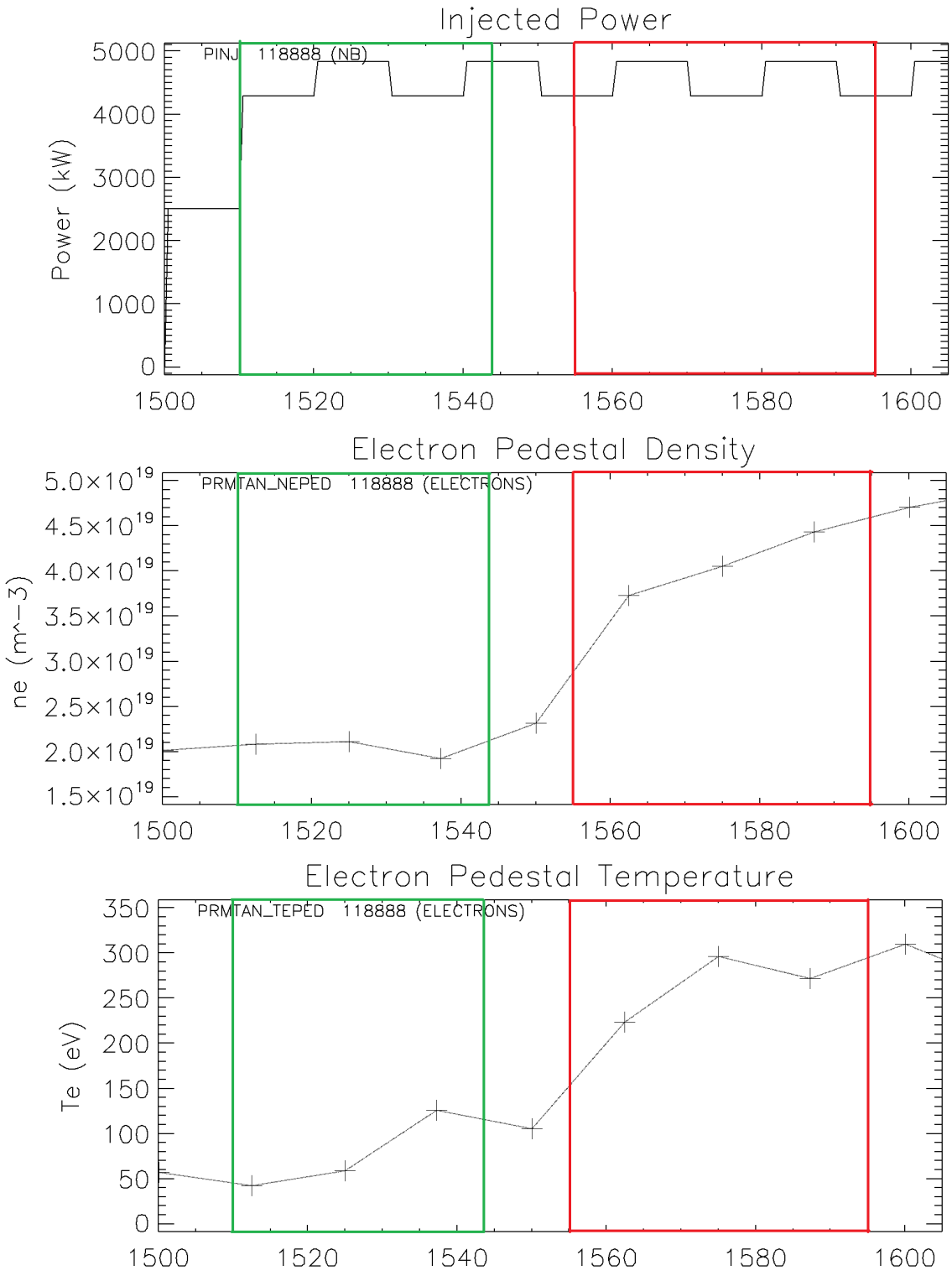

Figure A.2: Time dependent experimental data for shot #118888. The leftmost box is the L-mode time-slice, and the rightmost box is the H-mode time-slice

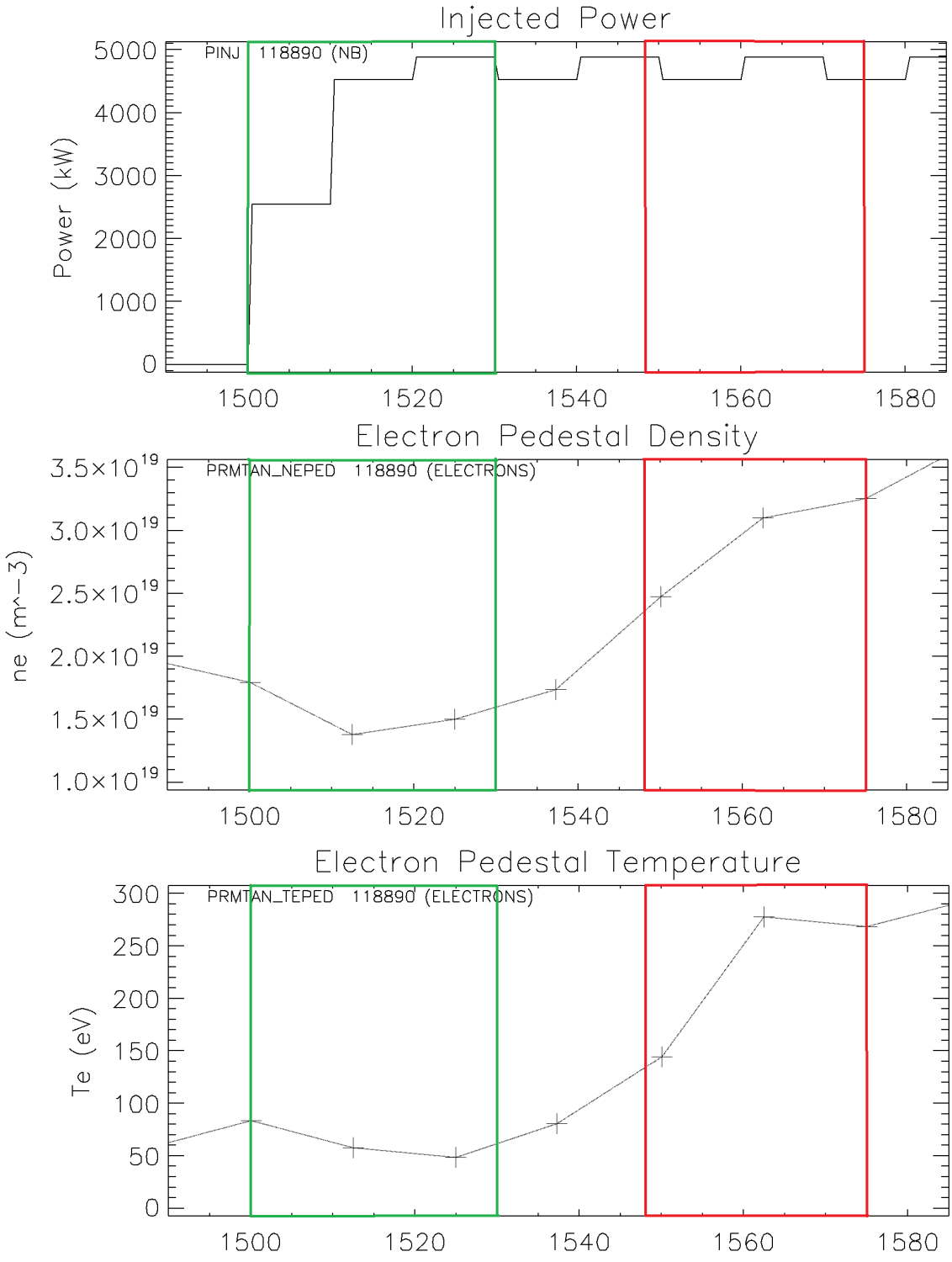

Figure A.3: Time dependent experimental data for shot #118890. The leftmost box is the L-mode time-slice, and the rightmost box is the H-mode time-slice

REFERENCES

[1] P. Agreement, "United nations framework convention on climate change," *Paris, France*, 2015.

[2] W. M. Stacey, *Fusion Plasma Physics*. Wiley-VCH, 2005.

[3] F. Wagner, G. Becker, K. Behringer, D. Campbell, A. Eberhagen, W. Engelhardt, G. Fussmann, O. Gehre, J. Gernhardt, G. v. Gierke, G. Haas, M. Huang, F. Karger, M. Keilhacker, O. Klüber, M. Kornherr, K. Lackner, G. Lisitano, G. G. Lister, H. M. Mayer, D. Meisel, E. R. Müller, H. Murmann, H. Niedermeyer, W. Poschenrieder, H. Rapp, H. Röhr, F. Schneider, G. Siller, E. Speth, A. Stäbler, K. H. Steuer, G. Venus, O. Vollmer, and Z. Yü, "Regime of improved confinement and high beta in neutral-beam-heated divertor discharges of the asdex tokamak," *Phys. Rev. Lett.*, vol. 49, pp. 1408–1412, 19 Nov. 1982.

[4] S.-I. Itoh and K. Itoh, "Model of L to H-mode transition in tokamak," *Phys. Rev. Lett.*, vol. 60, pp. 2276–2279, 22 May 1988.

[5] K.-C. Shaing, E. Crume Jr, and W. Houlberg, "Bifurcation of poloidal rotation and suppression of turbulent fluctuations: A model for the $L-H$ transition in tokamaks," *Physics of Fluids B: Plasma Phys. (1989-1993)*, vol. 2, no. 6, pp. 1492–1498, 1990.

[6] K. Burrell, "Effects of $E \times B$ velocity shear and magnetic shear on turbulence and transport in magnetic confinement devices," *Phys. Plasmas*, vol. 4, no. 5, pp. 1499–1518, 1997.

[7] P. Terry, "Suppression of turbulence and transport by sheared flow," *Reviews of Modern Physics*, vol. 72, no. 1, p. 109, 2000.

[8] W. M. Stacey, R. J. Groebner, and T. Evans, "Non-diffusive transport in the tokamak edge pedestal," *Nucl. Fusion*, vol. 52, no. 11, p. 114 020, 2012.

[9] W. Stacey, "Recent developments in plasma edge theory," *Contrib. to Plasma Phys.*, vol. 56, no. 6-8, pp. 495–503, 2016.

[10] ——, "Extended fluid transport theory in the tokamak plasma edge," *Nucl. Fusion*, vol. 57, no. 6, p. 066 034, 2017.

[11] J. L. Luxon, "A design retrospective of the diii-d tokamak," *Nucl. Fusion*, vol. 42, no. 5, p. 614, 2002.

[12] W. Stacey, M.-H. Sayer, J.-P. Floyd, and R. Groebner, "Interpretation of changes in diffusive and non-diffusive transport in the edge plasma during pedestal buildup following a low-high transition in diii-d," *Phys. Plasmas*, vol. 20, no. 1, p. 012 509, 2013.

[13] W. M. Stacey and R. J. Groebner, "Thermal transport analysis of the edge region in the low and high confinement stages of a diii-d discharge," *Phys. Plasmas*, vol. 14, no. 1, p. 012 501, 2007.

[14] ——, "Force balance and ion particle transport differences in high and low confinement tokamak edge pedestals," *Phys. Plasmas*, vol. 17, no. 11, p. 112 512, 2010.

[15] P. Gohil, K. H. Burrell, R. J. Groebner, J. Kim, W. C. Martin, E. L. McKee, and R. P. Seraydarian, "The charge exchange recombination diagnostic system on the diii-d tokamak," in *Proceedings of The 14th IEEE/NPSS Symposium Fusion Engineering*, vol. 2, 1991, pp. 1199–1204.

[16] R. Isler, "An overview of charge-exchange spectroscopy as a plasma diagnostic," *Plasma Physics and Controlled Fusion*, vol. 36, no. 2, p. 171, 1994.

[17] B. Grierson, K. Burrell, W. Heidbrink, M. Lanctot, N. Pablant, and W. Solomon, "Measurements of the deuterium ion toroidal rotation in the diii-d tokamak and comparison to neoclassical theory," *Physics of Plasmas*, vol. 19, no. 5, p. 056 107, 2012.

[18] T. N. Carlstrom, G. L. Campbell, J. C. DeBoo, R. Evanko, J. Evans, C. M. Greenfield, J. Haskovec, C. L. Hsieh, E. McKee, R. T. Snider, R. Stockdale, P. K. Trost, and M. P. Thomas, "Design and operation of the multipulse thomson scattering diagnostic on diii-d (invited)," *Review of Scientific Instruments*, vol. 63, no. 10, pp. 4901–4906, 1992.

[19] T. Osborne, P. Snyder, K. Burrell, T. Evans, M. Fenstermacher, A. Leonard, R. Moyer, M. Schaffer, and W. West, "Edge stability of stationary elm-suppressed regimes on diii-d," in *Journal of Physics: Conference Series*, IOP Publishing, vol. 123, 2008, p. 012 014.

[20] T. Carlstrom, K. Burrell, R. Groebner, A. Leonard, T. Osborne, and D. Thomas, "Comparison of lh transition measurements with physics models," *Nucl. Fusion*, vol. 39, no. 11Y, p. 1941, 1999.

[21] H. St. John, T. Taylor, Y. Lin-Liu, and A. Turnbull, "The charge exchange recombination diagnostic system on the diii-d tokamak," in *Proceedings of 15th IAEA Conference on Plasma Physics and Controlled Nuclear Fusion Research, Seville*, vol. 3, 1995, p. 60.

[22] W. M. Stacey, "A coupled plasma-neutrals model for divertor simulations," *Phys. Plasmas*, vol. 5, no. 4, pp. 1015–1026, 1998.

[23] W. Stacey, "Modelling the neutral density in the edge of the diii-d plasma," *Nucl. Fusion*, vol. 40, no. 5, p. 965, 2000.

[24] W. M. Stacey, "The effect of ion orbit loss and x-loss on the interpretation of ion energy and particle transport in the diii-d edge plasma," *Phys. Plasmas*, vol. 18, no. 10, p. 102 504, 2011.

[25] T. Wilks and W. Stacey, "Improvements to an ion orbit loss calculation in the tokamak edge," *Phys. Plasmas*, vol. 23, no. 12, p. 122 505, 2016.

[26] W. M. Stacey and M. T. Schumann, "The distribution of ion orbit loss fluxes of ions and energy from the plasma edge across the last closed flux surface into the scrape-off layer," *Phys. Plasmas*, vol. 22, no. 4, p. 042 504, 2015.

[27] K. Miyamoto, "Direct ion orbit loss near the plasma edge of a divertor tokamak in the presence of a radial electric field," *Nucl. Fusion*, vol. 36, no. 7, p. 927, 1996.

[28] J. Mandrekas, "Physics models and users guide for the neutral beam module of the supercode," Georgia Inst. of Tech., Atlanta, GA (United States). Fusion Research Center, Tech. Rep., 1992.

[29] W. M. Stacey and R. J. Groebner, "Interpretation of edge pedestal rotation measurements in diii-d," *Phys. Plasmas*, vol. 15, no. 1, p. 012 503, 2008.

[30] W. Stacey, "Ion particle transport in the tokamak edge plasma," *Contrib. to Plasma Phys.*, vol. 48, no. 1-3, pp. 94–98, 2008.

[31] B. Grierson, K. Burrell, W. Solomon, and N. Pablant, "Deuterium velocity and temperature measurements on the diii-d tokamaka)," *Review of Scientific Instruments*, vol. 81, no. 10, p. 10D735, 2010.

[32] W. M. Stacey and B. A. Grierson, "Interpretation of rotation and momentum transport in the diii-d edge plasma and comparison with neoclassical theory," *Nucl. Fusion*, vol. 54, no. 7, p. 073 021, 2014.

[33] S. Haskey, B. Grierson, K. Burrell, C Chrystal, R. Groebner, D. Kaplan, N. Pablant, and L Stagner, "Measurement of deuterium density profiles in the h-mode steep gradient region using charge exchange recombination spectroscopy on diii-d," *Review of Scientific Instruments*, vol. 87, no. 11, 11E553, 2016.